The Astrophysical Journal, 969:104 (24pp), 2024 July 10 https://doi.org/10.3847/1538-4357/ad4a72

Light-curve Structure and Hα Line Formation in the Tidal Disruption Event AT 2019azh

Sara Faris[1], Iair Arcavi[1], Lydia Makrygianni[1], Daichi Hiramatsu[2,3], Giacomo Terreran[4,5], Joseph Farah[4,5], D. Andrew Howell[4,5], Curtis McCully[4], Megan Newsome[4,5], Estefania Padilla Gonzalez[4,5], Craig Pellegrino[6], K. Azalee Bostroem[7,33], Wiam Abojanb[8], Marco C. Lam[9], Lina Tomasella[10], Thomas G. Brink[11], Alexei V. Filippenko[11], K. Decker French[12], Peter Clark[13], Or Graur[13,14], Giorgos Leloudas[15], Mariusz Gromadzki[16], Joseph P. Anderson[17,18], Matt Nicholl[19], Claudia P. Gutiérrez[20,21], Erkki Kankare[22], Cosimo Inserra[23], Lluís Galbany[20,21], Thomas Reynolds[22,24], Seppo Mattila[22,25], Teppo Heikkilä[22], Yanan Wang[26,27], Francesca Onori[28], Thomas Wevers[17,29], Eric R. Coughlin[30], Panos Charalampopoulos[31], and Joel Johansson[32]

[1] School of Physics and Astronomy, Tel Aviv University, Tel Aviv 69978, Israel; sarafaris452@gmail.com
[2] Center for Astrophysics, Harvard & Smithsonian, 60 Garden Street, Cambridge, MA 02138-1516, USA
[3] The NSF AI Institute for Artificial Intelligence and Fundamental Interactions, USA
[4] Las Cumbres Observatory, 6740 Cortona Drive, Suite 102, Goleta, CA 93117-5575, USA
[5] Department of Physics, University of California, Santa Barbara, CA 93106-9530, USA
[6] Department of Astronomy, University of Virginia, Charlottesville, VA 22904, USA
[7] Steward Observatory, University of Arizona, 933 North Cherry Avenue, Tucson, AZ 85721-0065, USA
[8] Atid Peki'in Comprehensive School, Peki'in, 2491400, Israel
[9] Institute for Astronomy, University of Edinburgh, Royal Observatory, Blackford Hill, Edinburgh, EH9 3HJ, UK
[10] INAF–Osservatorio Astronomico di Padova, Vicolo dell'Osservatorio 5, 35122 Padova, Italy
[11] Department of Astronomy, University of California, Berkeley, CA 94720-3411, USA
[12] Department of Astronomy, University of Illinois, 1002 W. Green Street, Urbana, IL 61801, USA
[13] Institute of Cosmology and Gravitation, University of Portsmouth, Portsmouth PO1 3FX, UK
[14] Department of Astrophysics, American Museum of Natural History, Central Park West and 79th Street, New York, NY 10024-5192, USA
[15] DTU Space, National Space Institute, Technical University of Denmark, Elektrovej 327, 2800 Kgs. Lyngby, Denmark
[16] Astronomical Observatory, University of Warsaw, Al. Ujazdowskie 4, 00-478 Warszawa, Poland
[17] European Southern Observatory, Alonso de Córdova 3107, Casilla 19, Santiago, Chile
[18] Millennium Institute of Astrophysics MAS, Nuncio Monsenor Sotero Sanz 100, Off. 104, Providencia, Santiago, Chile
[19] Astrophysics Research Centre, School of Mathematics and Physics, Queens University Belfast, Belfast BT7 1NN, UK
[20] Institut d'Estudis Espacials de Catalunya (IEEC), E-08034 Barcelona, Spain
[21] Institute of Space Sciences (ICE-CSIC), Campus UAB, Carrer de Can Magrans, s/n, E-08193 Barcelona, Spain
[22] Department of Physics and Astronomy, University of Turku, FI-20014 Turku, Finland
[23] Cardiff Hub for Astrophysics Research and Technology, School of Physics & Astronomy, Cardiff University, Queens Buildings, The Parade, Cardiff, CF24 3AA, UK
[24] Cosmic Dawn Center (DAWN), Niels Bohr Institute, University of Copenhagen, 2200, Denmark
[25] School of Sciences, European University Cyprus, Diogenes Street, Engomi, 1516 Nicosia, Cyprus
[26] National Astronomical Observatories, Chinese Academy of Sciences, 20A Datun Road, Beijing 100101, People's Republic of China
[27] Physics & Astronomy, University of Southampton, Southampton, Hampshire SO17 1BJ, UK
[28] INAF–Osservatorio Astronomico d'Abruzzo, via M. Maggini snc, I-64100 Teramo, Italy
[29] Space Telescope Science Institute, 3700 San Martin Drive, Baltimore, MD 21218, USA
[30] Department of Physics, Syracuse University, Syracuse, NY 13210, USA
[31] Department of Physics and Astronomy, University of Turku, Vesilinnantie 5, FI-20500, Finland
[32] Oskar Klein Centre, Department of Physics, Stockholm University, AlbaNova, SE-10691 Stockholm, Sweden
Received 2023 December 6; revised 2024 April 16; accepted 2024 April 17; published 2024 July 4

Abstract

AT 2019azh is a H+He tidal disruption event (TDE) with one of the most extensive ultraviolet and optical data sets available to date. We present our photometric and spectroscopic observations of this event starting several weeks before and out to approximately 2 yr after the *g*-band's peak brightness and combine them with public photometric data. This extensive data set robustly reveals a change in the light-curve slope and a possible bump in the rising light curve of a TDE for the first time, which may indicate more than one dominant emission mechanism contributing to the pre-peak light curve. Indeed, we find that the `MOSFiT`-derived parameters of AT 2019azh, which assume reprocessed accretion as the sole source of emission, are not entirely self-consistent. We further confirm the relation seen in previous TDEs whereby the redder emission peaks later than the bluer emission. The post-peak bolometric light curve of AT 2019azh is better described by an exponential decline than by the canonical $t^{-5/3}$ (and in fact any) power-law decline. We find a possible mid-infrared excess around the peak optical luminosity, but cannot determine its origin. In addition, we provide the earliest measurements of the Hα emission-

[33] LSSTC Catalyst Fellow.

line evolution and find no significant time delay between the peak of the *V*-band light curve and that of the Hα luminosity. These results can be used to constrain future models of TDE line formation and emission mechanisms in general. More pre-peak 1–2 days cadence observations of TDEs are required to determine whether the characteristics observed here are common among TDEs. More importantly, detailed emission models are needed to fully exploit such observations for understanding the emission physics of TDEs.

Unified Astronomy Thesaurus concepts: Accretion (14); Tidal disruption (1696); Supermassive black holes (1663); Ultraviolet transient sources (1854)

Supporting material: data behind figures, machine-readable table

1. Introduction

Supermassive black holes (SMBHs), with masses of $\gtrsim 10^6\,M_\odot$, are thought to reside in the center of most (if not all) large galaxies in the local Universe. While some SMBHs, known as active galactic nuclei (AGNs), accrete material that emits radiation, the majority are quiescent (e.g., Greene & Ho 2007; Mullaney et al. 2013) and thus difficult to study.

One of the few probes that can be used to study inactive SMBHs is the emission produced in a tidal disruption event (TDE). A TDE occurs when a star passes close enough to an SMBH for tidal forces to surpass the star's self-gravity, causing its disruption. In a full disruption, the star is torn apart and approximately half of it becomes gravitationally bound to the SMBH and eventually accretes onto it (Rees 1988; Evans & Kochanek 1989; Phinney 1989).

This transient phenomenon can not only serve to confirm the presence of an SMBH but also offers a promising tool for constraining its mass and perhaps even spin (e.g., Leloudas et al. 2016). As such, TDEs can potentially provide a more complete picture of the SMBH population. This can, in turn, help address some of the open questions regarding SMBHs, from accretion physics through their sub- and super-Eddington growth mechanisms to their scaling relations with global galaxy properties (such as the famous M–σ relation; e.g., Kormendy & Ho 2013). However, a main unresolved challenge lies in mapping TDE emission properties to SMBH characteristics.

The first discovered TDEs were searched for and detected in X-ray observations (e.g., Bade et al. 1996; Komossa & Greiner 1999; Cappelluti et al. 2009; Maksym et al. 2014; see Saxton et al. 2020 for a recent review), as the transient accretion disk was expected to emit at these wavelengths. However, in recent years, wide-field optical transient surveys have been discovering a growing number of TDEs in the optical bands, which are also bright in ultraviolet (UV) wavelengths (e.g., Gezari et al. 2006, 2012; van Velzen et al. 2011; Arcavi et al. 2014; see van Velzen et al. 2020 and Gezari 2021 for recent reviews). This surprising discovery has prompted work on theoretical models of TDEs to explain the optical/UV emission properties of these events.

Two main mechanisms for producing optical/UV emission in TDEs have been proposed. The first is the reprocessing of X-ray emission from an accretion disk by optically thick material surrounding the disk (e.g., Guillochon et al. 2014; Roth et al. 2016; Dai et al. 2018). The second model attributes the optical/UV emission to shocks formed between stellar debris streams as they collide around the apocenter before circularizing to form an accretion disk (Piran et al. 2015). Numerical simulations by Steinberg & Stone (2024) suggest a possible intermediate scenario whereby circularization can begin already at the pericenter, but the emission responsible for the light-curve peak is driven mainly by stream-disk shocks, which further circularizes the debris.

UV/optical TDEs are characterized by a luminous peak with a typical absolute magnitude of ~ -20 in the optical (a few events have been found down to peak magnitudes of ~ -17), rise timescales of days to weeks, and a smooth decline in the light curve lasting weeks to years (e.g., van Velzen et al. 2020, 2021). The blackbody temperature of these events remains high and approximately constant at $T \approx 10^4$ K (e.g., Gezari et al. 2012; Arcavi et al. 2014; van Velzen et al. 2020). Their bolometric luminosity sometimes follows a decline rate consistent with a $t^{-5/3}$ power law, which aligns with theoretical expectations for the mass return rate (Rees 1988; Evans & Kochanek 1989; Phinney 1989).

Spectroscopically, UV/optical TDEs show a strong blue continuum with broad ($\sim 10^4$ km s^{-1}) He II λ4686 (Gezari et al. 2012; Arcavi et al. 2014) and/or broad Balmer emission lines (e.g., Arcavi et al. 2014; Gezari et al. 2015; Hung et al. 2017), denoted H- He- or H+He-TDEs, accordingly (van Velzen et al. 2021). The width of the emission lines was initially attributed to Doppler broadening (Ulmer 1999; Bogdanović et al. 2004; Guillochon & Ramirez-Ruiz 2013). However, it was later suggested that at least some of the line broadening is caused by electron scattering (Roth & Kasen 2018). Some TDE spectra also exhibit He I λ5876 and/or heavier elements, such as [O III] λ5007 and N III $\lambda\lambda$4100, 4640 (sometimes blended with He II λ4686; Blagorodnova et al. 2017; Leloudas et al. 2019; Onori et al. 2019). Some of these lines have been attributed to the Bowen fluorescence mechanism (Bowen 1934), whereby extreme UV photons generate a specific cascade of lines. TDEs showing these lines are known as *Bowen TDEs*.

Some UV/optical TDEs are accompanied by X-ray and/or radio emission (e.g., Brown et al. 2017; Abolfathi et al. 2018; Saxton et al. 2020; Cendes et al. 2022; Liu et al. 2022; Bu et al. 2023). The X-rays are attributed to direct accretion emission, while the source of the radio emission is debated. It has been suggested to originate in outflows (Alexander et al. 2016), jets (van Velzen et al. 2016), and in the interaction between the unbound material and the interstellar medium (Krolik et al. 2016). In addition, delayed radio flares have recently been discovered to occur years after the optical peak in a few TDEs (Horesh et al. 2021). Their nature is also debated.

Here, we present and analyze extensive optical and UV observations, and available mid-infrared (MIR) observations, of the TDE AT 2019azh. X-ray, UV, and optical observations of this event were studied by Hinkle et al. (2021a), van Velzen et al. (2021), Liu et al. (2022), and Hammerstein et al. (2023), and long-duration radio emission by Goodwin et al. (2022) and Sfaradi et al. (2022). Spectropolarimetry of AT 2019azh was studied by Leloudas et al. (2022) and found to have the lowest polarization among the sample of TDEs studied.

We complement published optical and UV data of AT 2019azh with our own. The combined optical and UV data set presented here makes AT 2019azh one of the best-observed TDEs so far at these wavelengths, both photometrically and spectroscopically. We describe our observations in Section 2 and our analysis in Section 3, discuss our results in Section 4, and summarize in Section 5. We assume a flat ΛCDM cosmology, with $H_0 = 69.6\,\mathrm{km\,s^{-1}\,Mpc^{-1}}$, $\Omega_m = 0.286$, and $\Omega_\Lambda = 0.714$ (Wright 2006; Bennett et al. 2014).

2. Observations and Data Reduction

2.1. Discovery and Classification

AT 2019azh was discovered on 2019 February 22 at 00:28:48 (UTC dates are used throughout this paper) (MJD 58536.02; Stanek 2019) by the All-Sky Automated Survey for Supernovae (ASAS-SN; Shappee et al. 2014) as ASASSN-19dj with a *g*-band apparent magnitude of ∼16.2. The event was also detected by the Gaia photometric science alert team (Hodgkin et al. 2021)[34] as Gaia19bvo, and by the Zwicky Transient Facility (ZTF; Bellm et al. 2019) as ZTF17aaazdba and ZTF18achzddr.[35] The location of the event (Gaia J2000 coordinates $\alpha = 08^{\rm h}13^{\rm m}16\overset{\rm s}{.}96$, $\delta = +22°38'53\overset{''}{.}99$) is consistent with the center of the nearby galaxy KUG 0810+227, which has a redshift of $z = 0.0222240 \pm 0.0000071$ (Almeida et al. 2023), corresponding to a luminosity distance of 96.6 Mpc. This galaxy was preselected by French & Zabludoff (2018) as a possible TDE host, given its post-starburst properties (Arcavi et al. 2014).

The first few spectra of AT 2019azh showed a strong blue continuum without obvious features (Barbarino et al. 2019; Heikkila et al. 2019). The event was later classified as a TDE by van Velzen et al. (2019), based on its brightness, high blackbody temperature of ∼30,000 K, a position consistent with the center of the galaxy (with an angular offset between the ZTF coordinates of the event and the host nucleus of $0\overset{''}{.}07 \pm 0\overset{''}{.}31$), multiple spectra showing a strong blue continuum, and lack of spectroscopic features associated with a supernova (SN) or AGN.

2.2. Photometry

We obtained optical follow-up imaging of AT 2019azh with the Las Cumbres Observatory (Brown et al. 2013) global network of 1 m telescopes starting on MJD 58537.06 in the *BgVri* bands. Standard image processing was performed using the BANZAI automated pipeline (McCully et al. 2018). We combine our set of images with that of Hinkle et al. (2021a) and perform reference subtraction to remove host galaxy contamination using the High Order Transform of PSF and Template Subtraction algorithm (Alard & Lupton 1998; Alard 2000; Becker 2015) implemented by the `lcogtsnpipe` image subtraction pipeline (Valenti et al. 2016).[36] We use Las Cumbres Observatory images taken at MJD 59131.40 (∼596 days after discovery), after the transient faded, as references. Photometry was calibrated to the Sloan Digital Sky Survey (SDSS) Data Release 14 (Abolfathi et al. 2018) for the *gri* bands and to the AAVSO Photometric All-Sky Survey Data Release 9 (Henden et al. 2016) for the *BV* bands.

AT 2019azh was observed by all five ASAS-SN units in the *g* band, with the first detection recorded at MJD 58529.12. We use the ASAS-SN host-subtracted photometry as provided by Hinkle et al. (2021a).

The Swope (Bowen & Vaughan 1973) 1 m telescope at Las Campanas Observatory observed AT 2019azh in the *uBgVri* filters starting at MJD 58549.10. We use the Swope host-subtracted photometry as provided by Hinkle et al. (2021a).

We retrieved host-subtracted photometry from the Asteroid Terrestrial-impact Last Alert System (ATLAS; Tonry et al. 2018; Smith et al. 2020) in its *c* and *o* bands using the ATLAS public forced photometry server.[37] AT 2019azh was first detected by ATLAS on MJD 58529.37. More details regarding ATLAS data processing and photometry extraction can be found in Tonry et al. (2018) and Smith et al. (2020).

We retrieved ZTF host-subtracted photometry from the public ZTF forced photometry server.[38] The event was detected in the ZTF *g* and *r* bands starting from MJD 58512.26. A description of forced photometry processing for ZTF can be found in Masci et al. (2019).

The Neil Gehrels Swift Observatory (hereafter, Swift; Roming et al. 2005) observed AT 2019azh with all its UltraViolet and Optical Telescope (UVOT) filters (*b*, *v*, *u*, *uvw*1, *uvm*2, and *uvw*2), starting on MJD 58544.76 (PIs Arcavi, Hinkle, and Gezari). We take the host-subtracted extinction-corrected UVOT photometry from Hinkle et al. (2021b), which incorporates the new UVOT calibrations[39] not available in the earlier work by Hinkle et al. (2021a).

We retrieve the available MIR photometry obtained by the Wide-field Infrared Survey Explorer (WISE; Wright et al. 2010) NEOWISE Reactivation Releases (Mainzer et al. 2011, 2014) through the NASA/IPAC Infrared Science Archive. WISE obtains several images of each object during each observing phase (once every six months). We process these data using a custom Python script. The script filters out any individual observation identified as an upper limit and those with observational issues, such as being obtained close to the sky position of the Moon or suffering from poor frame quality. Weighted averages for each visit are then calculated per filter. We estimate the host galaxy flux and its uncertainty as the average and variance (respectively) of all pre-TDE observations and then subtract this flux from all observations.

We correct all optical and UV photometry for Milky Way extinction assuming a Cardelli et al. (1989) extinction law with $R_V = 3.1$ and Galactic extinction of $A_V = 0.122$ mag, as retrieved from the NASA Extragalactic Database[40] using the Schlafly & Finkbeiner (2011) extinction map. We correct the WISE MIR photometry for extinction using the Fitzpatrick (1999) extinction law with the corresponding coefficients from Yuan et al. (2013). All photometry is presented in the AB system (Oke 1974), except for the Las Cumbres *BV*-band data, which are presented in the Vega system.

The photometry obtained here from Las Cumbres, ATLAS, and ZTF are presented in Table 1. This photometry, together with the ASAS-SN and Swope photometry from Hinkle et al. (2021a), and the Swift photometry from Hinkle et al. (2021b),

[34] http://gsaweb.ast.cam.ac.uk/alerts

[35] The multiple names with prediscovery years are due to random image subtraction artifacts, which are common in galaxy nuclei, erroneously identified as possible transients.

[36] https://github.com/LCOGT/lcogtsnpipe

[37] https://fallingstar-data.com/forcedphot/

[38] https://ztfweb.ipac.caltech.edu/cgi-bin/requestForcedPhotometry.cgi

[39] https://www.swift.ac.uk/analysis/uvot/index.php

[40] https://ned.ipac.caltech.edu/extinction_calculator

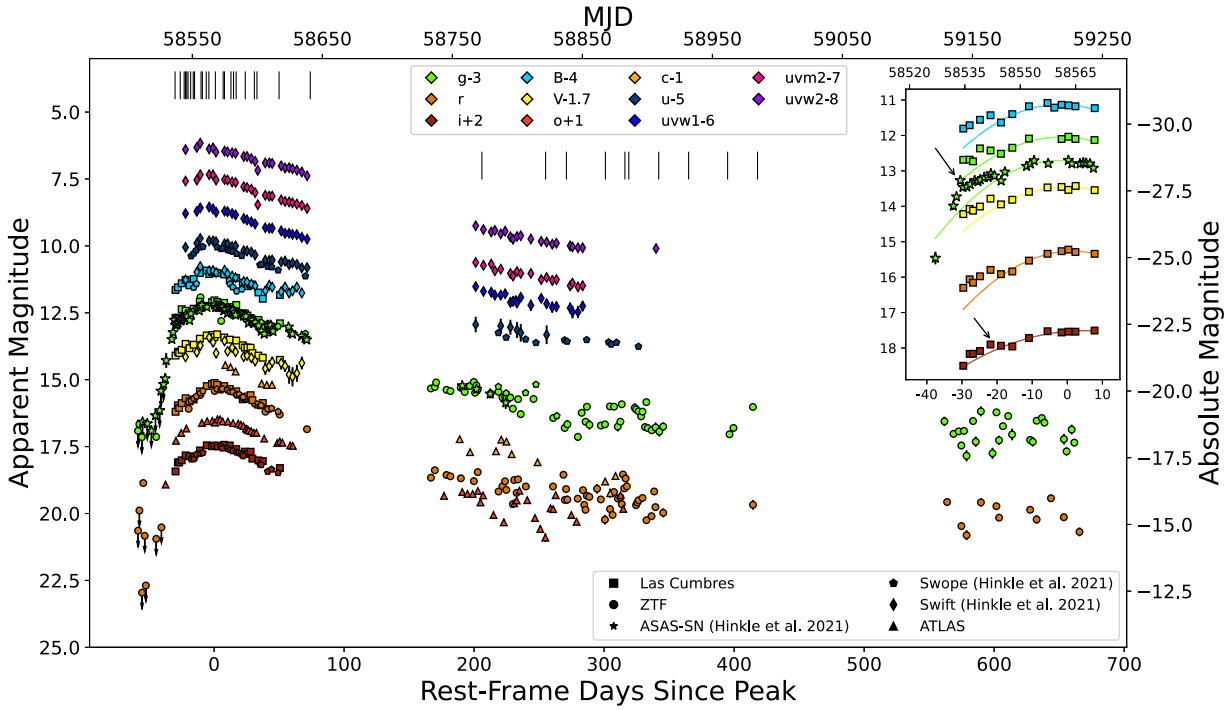

Figure 1. Milky Way extinction-corrected UV and optical light curves of AT 2019azh from Hinkle et al. (2021a, 2021b) and this work. Error bars denote 1σ uncertainties and are sometimes smaller than the marker size. Markers with arrows indicate 3σ nondetection upper limits. Black vertical lines indicate epochs with spectroscopic data. The inset displays the rise of the light curve in the data series, which covers the change in slope (at ~ -30 days from the peak) and possible bump (at ~ -20 days), marked with arrows (nondetections are omitted for clarity). The lines in the inset represent fits to the post-bump light curve, see the text for details.

Table 1
Host-subtracted and Milky Way Extinction-corrected Photometry and 3σ Nondetection Upper Limits

MJD	Phase (days)	Magnitude	Error	Filter	Source
58509.23	−55.93	>19.66	…	g	ZTF
58509.28	−55.88	>19.88	…	r	ZTF
58512.26	−52.90	18.86	0.05	*r*	ZTF
58522.18	−42.98	20.13	0.15	*g*	ZTF
58537.07	−28.09	16.19	0.02	*r*	Las Cumbres
58537.07	−28.09	15.69	0.09	*g*	Las Cumbres
58571.85	6.69	17.14	0.01	W1	WISE
58571.85	6.69	17.47	0.01	W2	WISE

(This table is available in its entirety in machine-readable form.)

is presented in Figure 1. The WISE photometry is also presented in Table 1 and in Figure A1 in Appendix A. We present all phases relative to *g*-band peak brightness at MJD 58566.70 ± 0.52 (as calculated in Section 3).

2.3. Spectroscopy

We obtained spectroscopic observations using the FLOYDS spectrographs (Sand et al. 2011) mounted on the Las Cumbres Observatory 2 m Faulkes Telescope South located at the Siding Spring Observatory in Australia and Faulkes Telescope North located at the Haleakalā Observatory in Hawaii, the ESO Faint Object Spectrograph and Camera (EFOSC2; Buzzoni et al. 1984) mounted on the 3.58 m ESO New Technology Telescope (NTT) as part of the extended Public ESO Spectroscopic Survey for Transient Objects (ePESSTO), the Asiago Faint Object Spectrographic Camera (AFOSC) mounted on the Copernico 1.82 m Telescope in Asiago, Mount Ekar, the Intermediate-dispersion Spectrograph and Imaging System (ISIS) mounted on the 4.2 m William Herschel Telescope (WHT), the Wide field reimaging CCD camera (WFCCD) mounted on the du Pont 2.5 m telescope at the Las Campanas Observatory, the Kast Double Spectrograph (Miller & Stone 1994) mounted on the Shane 3 m telescope at Lick Observatory, and the Alhambra Faint Object Spectrograph and Camera (ALFOSC) mounted on the 2.56 m Nordic Optical Telescope (NOT) through the second NOT Un-biased Transient Survey program.[41]

The FLOYDS spectra were processed and reduced using a custom `PYRAF`-based pipeline.[42] This pipeline, based on the `Image Reduction and Analysis Facility` (`IRAF`; Tody 1986, 1993) framework, removes cosmic rays and performs wavelength and flux calibration and rectification, flat-field correction, and spectrum extraction.

The Copernico 1.82 m Telescope spectra were reduced using a custom reduction pipeline based on IRAF tasks. After bias and flat-field correction, spectra were extracted and wavelength calibrated. Nightly sensitivity functions were derived from observations of spectrophotometric standard stars (also used to derive the corrections for the telluric absorption bands).

The NTT spectra were reduced using the Python-based `PESSTO` pipeline (Smartt et al. 2015).[43] This pipeline encompasses essential steps, including detector bias calibration, flat-field calibration, cosmic-ray removal, comparison lamp frames, and wavelength and flux calibrations. The first NTT

[41] https://nuts.sn.ie
[42] https://github.com/LCOGT/floyds_pipeline
[43] https://github.com/svalenti/pessto

spectrum, obtained on MJD 58539.16, is publicly available on the Transient Name Server[44] (Barbarino et al. 2019).

The WHT/ISIS spectrum was reduced using custom recipes executed in IRAF. The use of the medium-resolution gratings (R600B and R600R) results in a gap in wavelength coverage between the blue and red arms. Overscan correction, bias subtraction, flat-field correction, and cosmic-ray removal were performed. Wavelength calibration is derived from comparison lamp frames taken at the same position to correct instrument flexure. The optimal extraction algorithm of Horne (1986) is used to extract the one-dimensional spectra. A photometric standard star was observed on the same night to derive the flux calibration.

Observations with the WFCCD on the 2.5 m du Pont telescope were obtained using a 1.″65 (150 μm) slit and the blue grism. Average seeing conditions were ∼0.″5. Data were reduced and calibrated using custom Python routines and standard star observations.

The Lick/Kast spectra were taken with the 600/4310 grism, the 300/7500 grating, and the D57 dichroic. All observations were made with the 2.″0 slit. This instrument configuration has a combined wavelength range of ∼3600–10700 Å, and a spectral resolving power of $R \approx 800$. The data were reduced following standard techniques for CCD processing and spectrum extraction (Silverman et al. 2012) utilizing IRAF routines and custom Python and IDL codes.[45] Low-order polynomial fits to comparison lamp spectra were used to calibrate the wavelength scale, and small adjustments derived from night-sky lines in the target frames were applied. The spectra were flux calibrated and telluric corrected using observations of appropriate spectrophotometric standard stars observed on the same night, at similar airmasses, and with an identical instrument configuration.

The ALFOSC spectrum was reduced using the `foscgui`[46] pipeline. The pipeline performs overscan, bias, and flat-field corrections; spectrum extraction; wavelength calibration; flux calibration; and removal of telluric features with `IRAF` tasks as well as the removal of cosmic-ray artifacts using `lacosmic` (van Dokkum 2001).

All spectra were obtained with the slit oriented at or near the parallactic angle to minimize slit losses due to atmospheric dispersion (Filippenko 1982).

We retrieved the spectrum of the host galaxy from SDSS Data Release 18 (Almeida et al. 2023). The spectrum was obtained on 2003 October 30, and covers a wavelength range of 3700–9300 Å with a spectral resolution of $R \approx 2000$.

We calibrate all spectra of AT 2019azh (except for the WHT spectrum, owing to its wavelength gap) and that of the host galaxy to photometry and correct the TDE spectra for Milky Way extinction[47] using the `PySynphot` package (STScI Development Team 2013).[48]

A log of our spectroscopic observations is provided in Table 2; all spectra are presented in Figure 2 and will be made available through the Weizmann Interactive Supernova Data Repository (Yaron & Gal-Yam 2012).[49]

3. Analysis

3.1. Photometry

3.1.1. Light-curve Rise

The high-cadence pre-peak observations of AT 2019azh allow us to identify structure in its early optical light curve. First, we identify an abrupt change in the rising slope of the *g*-band light curve at ∼−30 days relative to the peak. We fit the rising *g*-band light curve with a linear function once between MJD 58520 and 58537, and once between MJD 58537 and 58560, finding a significant change in slope from 0.279 ± 0.014 mag day^{-1} in the first interval to 0.0323 ± 0.0042 mag day^{-1} in the second interval.

Second, a possible *bump* at ∼−20 days relative to the peak can be seen in the *BgVri* bands. While subtle, it is present in all bands that cover that epoch in the Las Cumbres and ASAS-SN data. We fit a second-order polynomial to the photometry after the bump, from −20 to 10 days relative to the peak, and plot it in the inset of Figure 1, extrapolating the fit to the bump epochs. The bump is clearly seen as an excess above this fit. Such structure was not previously robustly identified in a TDE, in part owing to the lack of high-cadence pre-peak observations for most events. However, indications for early light-curve structure were seen in at least two TDEs, which we discuss in Section 4.

3.1.2. Light-curve Peak

We fit a second-order polynomial to the host-subtracted Las Cumbres optical photometry and Swift UV photometry (except for the Swift *uvw*2 data, which does not cover enough of the rise to peak brightness) between MJD 58536 and 58596 to determine the peak time and magnitude in each band (the fits are displayed in Figure B1 in Appendix B). The best-sampled light curve around the peak is that in the *g* band for which we find a peak time of MJD 58566.70 ± 0.52 and a peak absolute magnitude of -19.82 ± 0.03. We use this peak time as a reference for all phase information in this paper. We also check the cross-correlation offset between the *g* light curve and the light curves in the bands mentioned above, in the same time range, using the `PyCCF` package[50] (Peterson et al. 1998).

Table 3 details the peak time and apparent magnitude from the fit to peak in each band. Figure 3 illustrates the peak times of each band in relation to their central wavelengths. The *uvm*2, *uvw*1, and *u*-band central wavelengths and filter widths are taken from Poole et al. (2008), while the central wavelengths and filter widths for the rest of the bands are from the Las Cumbres Observatory website.[51] We find consistent results between the peak time fit method and the cross-correlation method. Both show a monotonic peak time versus wavelength relation (also found in other TDEs; see Section 4), with the peak-fit method results having a Pearson correlation coefficient of 0.993, and a best-fit linear slope of $(2.16 \pm 0.10) \times 10^{-3}$ day Å^{-1}.

We find a significant MIR flare at 5.15 days after the *g*-band peak, with a W1 − W2 color of −0.32 mag, which is well

[44] http://www.wis-tns.org/

[45] https://github.com/ishivvers/TheKastShiv

[46] foscgui is a graphical user interface aimed at extracting SN spectroscopy and photometry obtained with FOSC-like instruments. It was developed by E. Cappellaro. A package description can be found at http://sngroup.oapd.inaf.it/foscgui.html.

[47] The host galaxy spectrum was already corrected for Milky Way extinction, assuming the Cardelli et al. (1989) extinction law and using the all-sky dust maps from Pan-STARRS (Green et al. 2018).

[48] https://pysynphot.readthedocs.io/en/latest/

[49] https://www.wiserep.org

[50] http://ascl.net/1805.032

[51] https://lco.global/observatory/instruments/filters/

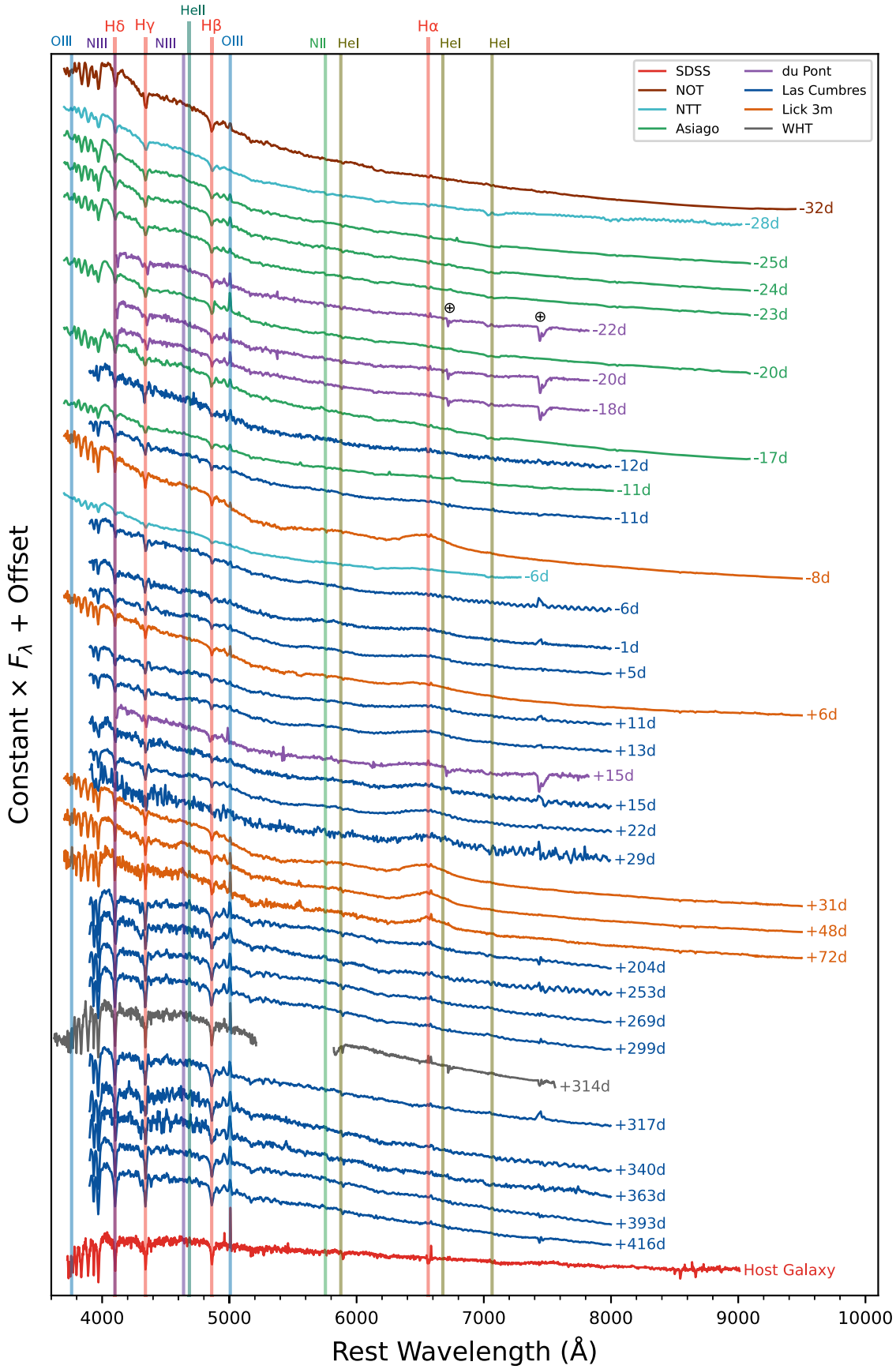

Figure 2. Spectroscopic evolution of AT 2019azh and the archival host galaxy spectrum from SDSS, after photometric calibration and Galactic extinction correction (except for the WHT spectrum). Notable TDE features, such as broad Hα and He II λ4686 emission lines, are evident in the spectra. We attribute the narrow Balmer absorption and narrow [O III] λ5007 emission lines, seen in all spectra, to the host galaxy. The phase of each spectrum in rest-frame days relative to the g-band light-curve peak is indicated and telluric lines are marked.

Table 2
Log of Spectroscopic Observations

Phase (days)	Telescope/Instrument	Slit Width (″)	Exposure Time (s)
−32	NOT/ALFOSC	1.3	900
−28	NTT/EFOSC2	1	300
−25	Copernico/AFOSC	1.69	1800
−24	Copernico/AFOSC	1.69	1500
−23	Copernico/AFOSC	1.69	1200
−22	du Pont/WFCCD	1.65	2700
−20	Copernico/AFOSC	1.69	2400
−20	du Pont/WFCCD	1.65	2700
−18	du Pont/WFCCD	1.65	2700
−17	Copernico/AFOSC	1.69	1800
−12	Las Cumbres/FLOYDS	2	1200
−11	Las Cumbres/FLOYDS	2	1200
−11	Copernico/AFOSC	1.69	2700
−8	Lick 3 m/Kast	2	2400
−6	NTT/EFOSC2	1	900
−6	Las Cumbres/FLOYDS	2	1200
−1	Las Cumbres/FLOYDS	2	1200
+5	Las Cumbres/FLOYDS	2	1200
+6	Lick 3 m/Kast	2	2400
+11	Las Cumbres/FLOYDS	2	1200
+13	Las Cumbres/FLOYDS	2	1200
+15	Las Cumbres/FLOYDS	2	1200
+15	du Pont/WFCCD	1.65	2700
+22	Las Cumbres/FLOYDS	2	1200
+29	Las Cumbres/FLOYDS	2	1200
+31	Lick 3 m/Kast	2	1500
+48	Lick 3 m/Kast	2	1800
+72	Lick 3 m/Kast	2	1800
+204	Las Cumbres/FLOYDS	2	3600
+253	Las Cumbres/FLOYDS	2	3600
+269	Las Cumbres/FLOYDS	2	3600
+299	Las Cumbres/FLOYDS	2	3600
+314	WHT/ISIS	1	2700
+317	Las Cumbres/FLOYDS	2	3600
+340	Las Cumbres/FLOYDS	2	3600
+363	Las Cumbres/FLOYDS	2	3600
+393	Las Cumbres/FLOYDS	2	3600
+416	Las Cumbres/FLOYDS	2	3600

Note. Phase is given in rest-frame days from the *g*-band peak brightness.

below the AGN threshold of $W1 - W2 = 0.8$ determined by Stern et al. (2012).

We calculate the expected MIR flux of a blackbody with the best-fit temperature and radius from day 8.09 after the *g*-band peak (the closest blackbody fit to the time of the WISE detections; see Section 3.1.3) using the `synphot` package (STScI Development Team 2018) with the WISE W1 and W2 filter bandpasses from Wright et al. (2010). We find that such a blackbody would produce a W1 and W2 AB magnitude of -16.32 ± 0.07 (the difference between the W1 and W2 magnitudes is negligible at the assumed temperature of $2.46 \pm 0.15 \times 10^4$ K derived in Section 3.1.3). The MIR detection extinction-corrected W1 and W2 AB magnitudes are -17.76 ± 0.13 and -17.45 ± 0.11, respectively, which are ∼1.1–1.5 mag brighter than the blackbody emission inferred from the optical and UV data. This excess may be due to a prompt dust echo, as observed, for example, by Newsome et al. (2024), but we cannot verify this without further data. We leave further analysis of the MIR emission from AT 2019azh to future work.

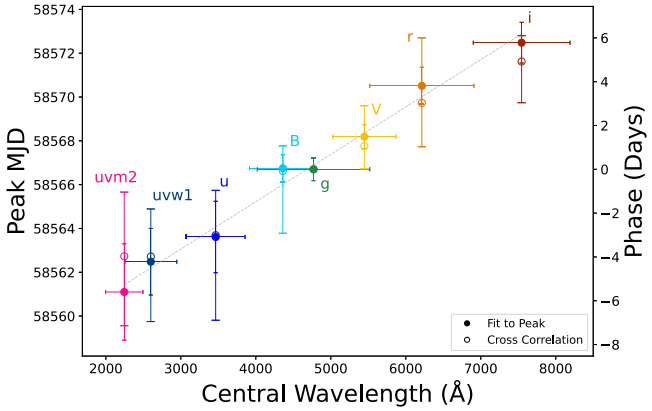

Figure 3. Light-curve peak MJD in various bands. Bluer bands peak earlier than redder bands. Filter widths are indicated with horizontal lines. The dashed gray line indicates a linear fit to the data.

3.1.3. Blackbody Fits

We fit the UV/optical photometry of AT 2019azh with a blackbody spectrum through the `SuperBol` fitting package[52] (Nicholl 2018), which uses the least-squares fitting method.[53] Here, we exclude ATLAS observations since the *c*- and *o*-band filters overlap with other filters, making them not fully independent observations. We restrict the fitting to epochs with available UV observations, as this helps reduce systematic errors when fitting blackbodies hotter than ∼30,000 K with optical data alone (Arcavi 2022), while linearly interpolating the optical light curves where necessary. We then calculate the bolometric luminosity using the Stefan–Boltzmann law, $L_{\rm bol} = 4\pi R^2 \sigma_{\rm SB} T^4$, with $\sigma_{\rm SB}$ the Stefan–Boltzmann constant, and R and T the blackbody radius and temperature from the fit, respectively.[54]

The evolution of the blackbody temperature, radius, and resulting bolometric luminosity are given in Table 4 and presented in Figure 4 in comparison to 15 other TDEs from van Velzen et al. (2021).[55] As with other TDEs, AT 2019azh exhibits constant high (∼25,000 K) temperatures with values at the high end, but consistent with the sample of van Velzen et al. (2021). Its blackbody radius evolution is also consistent with that of other TDEs and falls in the middle of the comparison sample. The bolometric luminosity of AT 2019azh is on the high end of the comparison sample, but still consistent with it. Our results are also roughly consistent with those of Hinkle et al. (2021b), but we obtain slightly lower temperatures and bolometric luminosities, especially at late times, compared to them.

We fit the post-peak bolometric light curve with a power law of the form $L \propto \left(\frac{t - t_0}{\tau}\right)^{-\alpha}$ and an exponential decline of the form $L \propto e^{-\frac{t-t_0}{\tau}}$. We perform the power-law fit in three

[52] https://superbol.readthedocs.io/en/latest/

[53] We convert the UVOT magnitudes to the Vega system, as required by SuperBol, using the conversions in https://swift.gsfc.nasa.gov/analysis/uvot_digest/zeropts.html.

[54] Here, we are not including any X-ray emission outside of the blackbody inferred from the optical and UV flux. Such emission is negligible around optical peak but comparable to what we measure at late times (Hinkle et al. 2021a).

[55] We compare to this sample since it is one of the largest samples of homogeneously analyzed TDE photometry to date.

Table 3
Peak MJD and Magnitude, Determined by Fitting a Second-order Polynomial to the Las Cumbres and Swift UV Photometry Around Peak Brightness

Band	Central Wavelength (Å)	Filter Width (Å)	Peak MJD	Phase (days)	Peak Magnitude	Cross-correlation Delay (days)
uvm2	2246	498	58561.10 ± 2.20	-4.70 ± 2.30	-20.49 ± 0.02	$-3.97^{+3.17}_{-2.93}$
uvw1	2600	693	58562.48 ± 1.52	-4.22 ± 1.66	-20.30 ± 0.02	$-3.98^{+2.97}_{-2.05}$
u	3465	785	58563.61 ± 1.63	-3.16 ± 1.77	-20.09 ± 0.02	$-3.01^{+3.88}_{-2.05}$
B	4361	890	58566.75 ± 0.61	0.05 ± 0.92	-19.91 ± 0.02	$-0.08^{+2.84}_{-1.15}$
g	4770	1500	58566.70 ± 0.52	0	-19.82 ± 0.03	0
V	5448	840	58568.19 ± 0.54	1.49 ± 0.87	-19.83 ± 0.02	$1.06^{+1.04}_{-1.84}$
r	6215	1390	58570.51 ± 0.85	3.81 ± 1.09	-19.68 ± 0.03	$3.03^{+2.00}_{-2.97}$
i	7545	1290	58572.48 ± 0.93	5.78 ± 1.15	-19.47 ± 0.02	$4.92^{+1.88}_{-1.18}$

Note. Phases are given relative to the *g*-band peak, and cross-correlation delays are given relative to the *g* light curve.

Table 4
Blackbody Temperature and Radius, and Resulting Bolometric Luminosity

Phase	T_{BB} (10^4 K)	R_{BB} (10^{14} cm)	L_{bol} (10^{44} erg s^{-1})
–21.94	2.55 ± 0.13	7.45 ± 0.43	1.66 ± 0.40
–13.25	2.75 ± 0.15	7.05 ± 0.45	2.03 ± 0.52
–10.59	2.83 ± 0.16	7.33 ± 0.45	2.46 ± 0.62
–3.75	2.49 ± 0.10	8.08 ± 0.38	1.80 ± 0.33
–0.76	2.55 ± 0.12	7.91 ± 0.43	1.88 ± 0.40
1.37	2.54 ± 0.17	7.70 ± 0.63	1.77 ± 0.56
1.58	2.36 ± 0.16	7.98 ± 0.68	1.42 ± 0.45
8.09	2.46 ± 0.15	7.87 ± 0.56	1.61 ± 0.45
10.40	2.43 ± 0.15	7.93 ± 0.59	1.55 ± 0.44
13.92	2.51 ± 0.18	7.38 ± 0.63	1.55 ± 0.51
16.57	2.50 ± 0.17	7.36 ± 0.61	1.51 ± 0.49
22.83	2.56 ± 0.18	6.71 ± 0.56	1.38 ± 0.45
25.35	2.62 ± 0.19	6.46 ± 0.55	1.40 ± 0.47
28.66	2.68 ± 0.22	6.06 ± 0.57	1.34 ± 0.50
31.59	2.63 ± 0.21	5.93 ± 0.55	1.19 ± 0.44
33.64	2.10 ± 0.17	7.00 ± 0.70	0.68 ± 0.26
39.42	2.94 ± 0.28	4.93 ± 0.51	1.29 ± 0.56
42.47	2.97 ± 0.32	4.85 ± 0.56	1.30 ± 0.64
44.72	2.54 ± 0.19	5.91 ± 0.47	1.03 ± 0.35
51.63	2.85 ± 0.25	4.86 ± 0.47	1.10 ± 0.45
54.62	2.81 ± 0.25	4.79 ± 0.47	1.02 ± 0.41
57.74	2.98 ± 0.25	4.45 ± 0.40	1.10 ± 0.42
60.33	3.00 ± 0.28	4.34 ± 0.44	1.08 ± 0.45
63.72	3.02 ± 0.29	4.21 ± 0.44	1.05 ± 0.46
67.50	3.05 ± 0.26	4.03 ± 0.38	1.00 ± 0.39
71.57	2.84 ± 0.23	4.19 ± 0.38	0.81 ± 0.30
201.24	3.13 ± 0.40	1.49 ± 0.19	0.15 ± 0.09
220.51	2.88 ± 0.29	1.44 ± 0.15	0.10 ± 0.05
223.89	2.73 ± 0.28	1.52 ± 0.16	0.09 ± 0.04
227.94	2.32 ± 0.16	1.76 ± 0.14	0.06 ± 0.02
232.99	2.60 ± 0.33	1.52 ± 0.21	0.08 ± 0.04
260.19	2.68 ± 0.56	1.25 ± 0.26	0.06 ± 0.05
275.68	2.62 ± 0.39	1.26 ± 0.19	0.05 ± 0.04
283.51	2.63 ± 0.38	1.23 ± 0.19	0.05 ± 0.03

Note. Phases are given relative to *g*-band peak brightness.

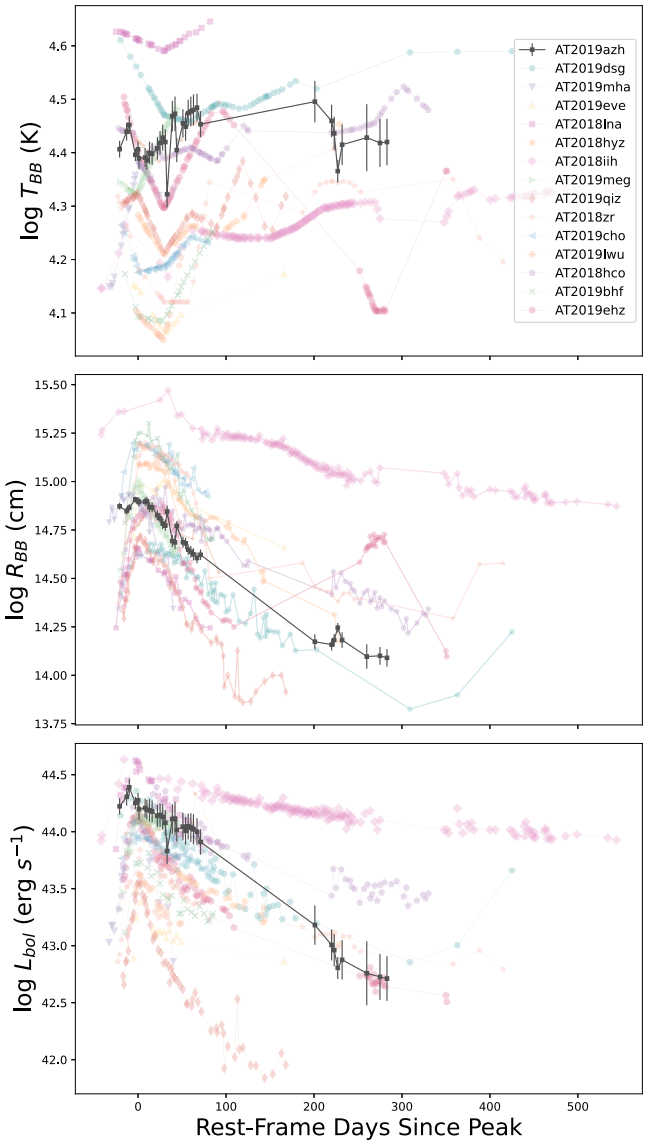

Figure 4. Blackbody temperature (top), radius (middle), and inferred bolometric luminosity (bottom) evolution obtained using `SuperBol` for AT 2019azh (black), compared to a sample of TDEs from van Velzen et al. (2021). The temperature, radius, and bolometric luminosity of AT 2019azh are consistent with those of other UV/optical TDEs. The van Velzen et al. (2021) measurements assume a parametric time evolution and hence are smoother.

(The data used to create this figure are available.)

different ways: once with the power-law index fixed to the canonical $\alpha = 5/3$ value and free t_0, once with free α and fixed t_0 (set to the best-fit value of -60 days from the peak, found by MOSFiT below), and once with free α and free t_0. The latter fit requires an unphysical t_0 of order 10^5 days before the peak to match the data, and the other two power-law fits (yielding

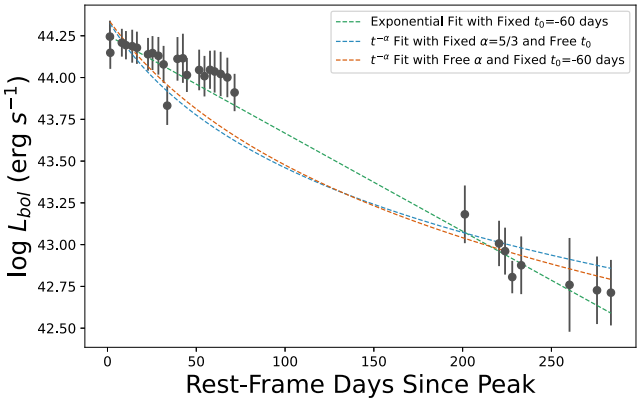

Figure 5. Power-law and exponential fits to the bolometric luminosity decline. The data are better represented by an exponential decline rather than a power law.

$\alpha = 2.06 \pm 0.11$ and $t_0 = -41.49 \pm 5.87$ days) are unable to match the data at all. The exponential decline, on the other hand, does match the data well. The different fits are shown in Figure 5. We conclude that the bolometric light-curve decline of AT 2019azh is better described by an exponential than a power law, similar to what was seen for ASASSN-15oi (Holoien et al. 2016a) and iPTF16fnl (Blagorodnova et al. 2017). Specifically, it does not fit the canonical $t^{-5/3}$ decline quoted for some TDEs.

3.1.4. TDE Model Fits

As mentioned in Section 1, there are currently two main models for the source of UV/optical emission in TDEs: reprocessing of X-rays from a rapidly formed accretion disk, and shock emission from debris stream collisions during the circularization process. We fit our photometry to the X-ray reprocessing model with the Modular Open Source Fitter for Transients (MOSFiT; Guillochon et al. 2018), and to the stream collision model with the TDEMass package (Ryu et al. 2020).

The MOSFiT TDE model (Mockler et al. 2019) is based on hydrodynamical simulations for converting the mass-fallback rate from the disrupted star to a bolometric flux. This conversion is related to the accretion rate through the viscous timescale $T_{\rm viscous}$, and it assumes a constant efficiency parameter ϵ. The reprocessing layer is assumed to be a simple blackbody photosphere with radius $R_{\rm phot}$.

The free parameters of the model are the BH mass ($M_{\rm BH}$); the mass of the disrupted star ($M_\star$); the viscous timescale ($T_{\rm viscous}$); the efficiency (ϵ); the blackbody photospheric radius $R_{\rm phot} \propto R_{\rm ph,0} \times L^{\,l}$ (where $R_{\rm ph,0}$ and l are free parameters and L is the bolometric luminosity); the scaled impact parameter (b), which is a proxy for the physical impact parameter $\beta \equiv R_{\rm t}/R_{\rm p}$ (with $R_{\rm t}$ the tidal radius and $R_{\rm p}$ the orbit pericenter); the time of first fallback ($t_{\rm exp}$); the host galaxy column density ($n_{\rm H}$); and a white-noise parameter (σ). We use the default priors from MOSFiT, as given by Mockler et al. (2019).

We utilize the nested sampling method,[56] implemented by DYNESTY (Speagle 2020), for the fit. As with the blackbody fits, here we also exclude the ATLAS bands. We further exclude observations more than 1 yr after discovery because the assumption of a blackbody photosphere made by MOSFiT might not be valid at such late times if the reprocessing material starts to become optically thin. We use the default MOSFiT termination criterion of a potential scale reduction factor of 1.1.

No formal goodness of fit metric is produced by this fitting procedure. The model matches the observations reasonably well in some regions and deviates from the data in others, as can be seen in Figure 6. Table 5 presents the best-fit parameters obtained from the fit; the posterior distributions, which are well converged, are displayed in Figure C1 in Appendix C. The efficiency parameter approaches its maximum allowed value, which affects the stellar mass parameter owing to their degeneracy (Mockler & Ramirez-Ruiz 2021). The impact parameter is $b = 0.99^{+0.01}_{-0.03}$, suggesting that the star is almost fully disrupted.

As Mockler et al. (2019) pointed out, this model includes several simplifications of the complex physics involved. For instance, assuming solar-composition polytropes instead of more realistic stellar density profiles that take into account the stellar metallicity, age, and evolutionary stage, could introduce systematic uncertainties in determining the stellar mass. Mockler et al. (2019) quantified these and other systematic uncertainties arising from some of the model simplifications, and we include these uncertainties in the total error estimates in Table 5.

In TDEMass (Ryu et al. 2020),[57] the mass of the disrupted star and the disrupting SMBH are estimated by numerically solving two nonlinear equations (Equations (11) and (12) of Ryu et al. 2020) and interpolating within precalculated tables of the peak bolometric luminosity ($L_{\rm obs}$) and the temperature at this peak ($T_{\rm obs}$). The equations include two parameters that determine the size and energy dissipation area of the emitting region: c_1, related to the apocenter distance for the orbit of the most tightly bound debris, and $\Delta\Omega$, the solid angle of the area where shocks dissipate a significant amount of energy. The values of these parameters are not well constrained, and the default model values of $c_1 = 1$ and $\Delta\Omega = 2\pi$ are assumed.

From our SuperBol fit, we find a peak luminosity of $L_{\rm obs} = 2.46 \pm 0.62 \times 10^{44}$ erg s^{-1} and a temperature at this peak of $T_{\rm obs} = 28{,}300 \pm 1550$ K. With these values, we obtain from TDEMass a BH mass of $M_{\rm BH} = 2.5^{+0.29}_{-0.24} \times 10^6\ M_\odot$ and a stellar mass of $M_\star = 4.8^{+4}_{-2.5}\ M_\odot$. Figure D1 in Appendix D displays the degeneracy between these two parameters. We

Table 5
Best-fit Parameters Obtained from the MOSFiT Fit with 1σ Confidence Intervals

Parameter	Best-fit Value	Total Error	Units
$\log(M_{\rm BH})$	$7.21^{+0.02}_{-0.02}$	± 0.20	$M_\odot$
$M_\star$	$0.1000^{+0.0002}_{-0.0002}$	± 0.66	$M_\odot$
$\log(T_{\rm viscous})$	$0.44^{+0.14}_{-0.42}$	± 0.43	day
$\log(\epsilon)$	$-0.47^{+0.05}_{-0.08}$	± 0.68	⋯
$\log(R_{\rm ph,0})$	$0.38^{+0.07}_{-0.05}$	± 0.4	⋯
l	$1.72^{+0.05}_{-0.06}$	± 0.2	⋯
b	$0.99^{+0.01}_{-0.03}$	± 0.35	⋯
$t_{\rm exp}$	$-6.95^{+1.24}_{-1.00}$	± 15	day
$\log(n_{\rm H})$	$20.66^{+0.03}_{-0.04}$	⋯	cm^{-2}
$\log(\sigma)$	$-0.45^{+0.01}_{-0.01}$	⋯	⋯

Note. The "Total Error" column includes systematic errors estimated by Mockler et al. (2019) due to some of the simplifying assumptions in the model.

[56] This method is typically employed for models with 10 or more parameters, as is the case here.

[57] https://github.com/taehoryu/TDEmass

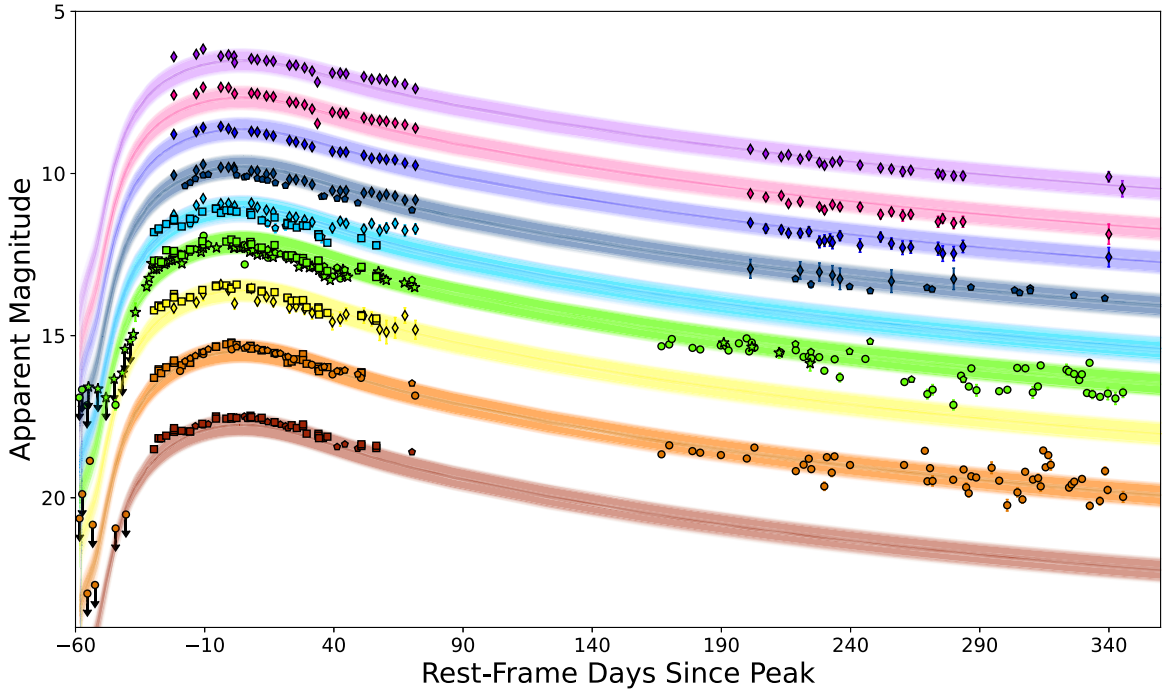

Figure 6. MOSFiT nested sampling fits to AT 2019azh photometry. Solid lines represent the medians of samples of light curves, while the shaded regions indicate the variance within each sample of models. Overall, the ensembles of models provide a reasonably good fit to the photometric data, but the best-fit parameters are not fully self-consistent (see Section 4.6). Arrows indicate 3σ nondetection upper limits. Colors, markers, and offsets are the same as in Figure 1.

compare these results to those found through MOSFiT in Section 4, though we do not expect them to agree since each model assumes a different emission mechanism responsible for the observed light curve.

3.2. Spectroscopy

3.2.1. Coronal Emission Lines

We use a custom analysis code (Clark et al. 2024, in preparation) to check for the presence of narrow [Fe VII], [Fe X], [Fe XI], and [Fe XIV] coronal emission lines in our spectra. Such lines are seen in extreme coronal line emitters (e.g., Komossa et al. 2008; Wang et al. 2012; Yang et al. 2013), a subset of which is associated with TDEs (e.g., Onori et al. 2022; Short et al. 2023; Callow et al. 2024; Clark et al. 2024) occurring in gas-rich environments. We find no significant evidence for such features in any of our spectra.

3.2.2. Other Emission Lines

To identify and study the broad emission lines, we follow the spectral analysis process outlined by Charalampopoulos et al. (2022) for removing host galaxy and continuum contributions to the emission line profiles (after performing the photometric calibration and Galactic extinction correction as detailed in Section 2). We exclude from this analysis the du Pont spectra to avoid telluric contamination, and all spectra taken after the seasonal gap (day 205 after peak and onward) given that the broad emission lines are very weak at such late times.

First, we subtract the host galaxy spectrum from each TDE spectrum after resampling the host spectrum to the wavelengths of the TDE spectrum using the SciPy interp1d function.[58] Since different spectra are taken under different seeing conditions, and the TDE spectra are taken with varying slit widths and angles, while the SDSS host spectrum was obtained through a fiber, there will be different host galaxy contributions to each TDE spectrum. Thus, it is impossible to completely remove host galaxy emission from the TDE spectra. Here, we attempt to minimize host galaxy contamination, but some residuals likely remain (see below).

Next, we identify line-free regions in the host-subtracted spectra to fit and remove the spectral continuum using a third-order polynomial. We use the line-free regions outlined by Charalampopoulos et al. (2022) as a basis, while tailoring them to match the AT 2019azh spectra. The selected line-free rest-frame wavelength ranges are 3900–4000, 4220–4280, 5100–5550, 6000–6100, and 6800–7000 Å.

An example of this spectral processing procedure, as performed on the spectrum from 13 days after peak brightness, is provided in Figure E1 in Appendix E. All spectra after host and continuum removal, for which this process was conducted, are presented in Figure E2 in Appendix E.

Broad emission lines of Hα, He II λ4686, and He I λ5876 are evident, as in other UV/optical TDEs (e.g., Gezari et al. 2012; Arcavi et al. 2014; Holoien et al. 2016b). The broad He II λ4686 emission line appears already in the first spectrum, remains relatively strong and broad until the seasonal gap at 72 days after the light-curve peak, and weakens in the spectra obtained after the gap (see Figure E2 in Appendix E). The broad Hα emission line strengthens at early times and later significantly weakens and narrows in the post-seasonal gap spectra. This behavior was observed in some other TDEs (e.g., Gezari et al. 2012; Holoien et al. 2014b, 2016b), and is discussed further in Section 3.2.3.

In addition to the broad emission lines, narrow Balmer Hβ and Hγ emission lines are seen in the host- and continuum-subtracted spectra. These lines likely originate from

[58] https://docs.scipy.org/doc/scipy/reference/generated/scipy.interpolate.interp1d.html

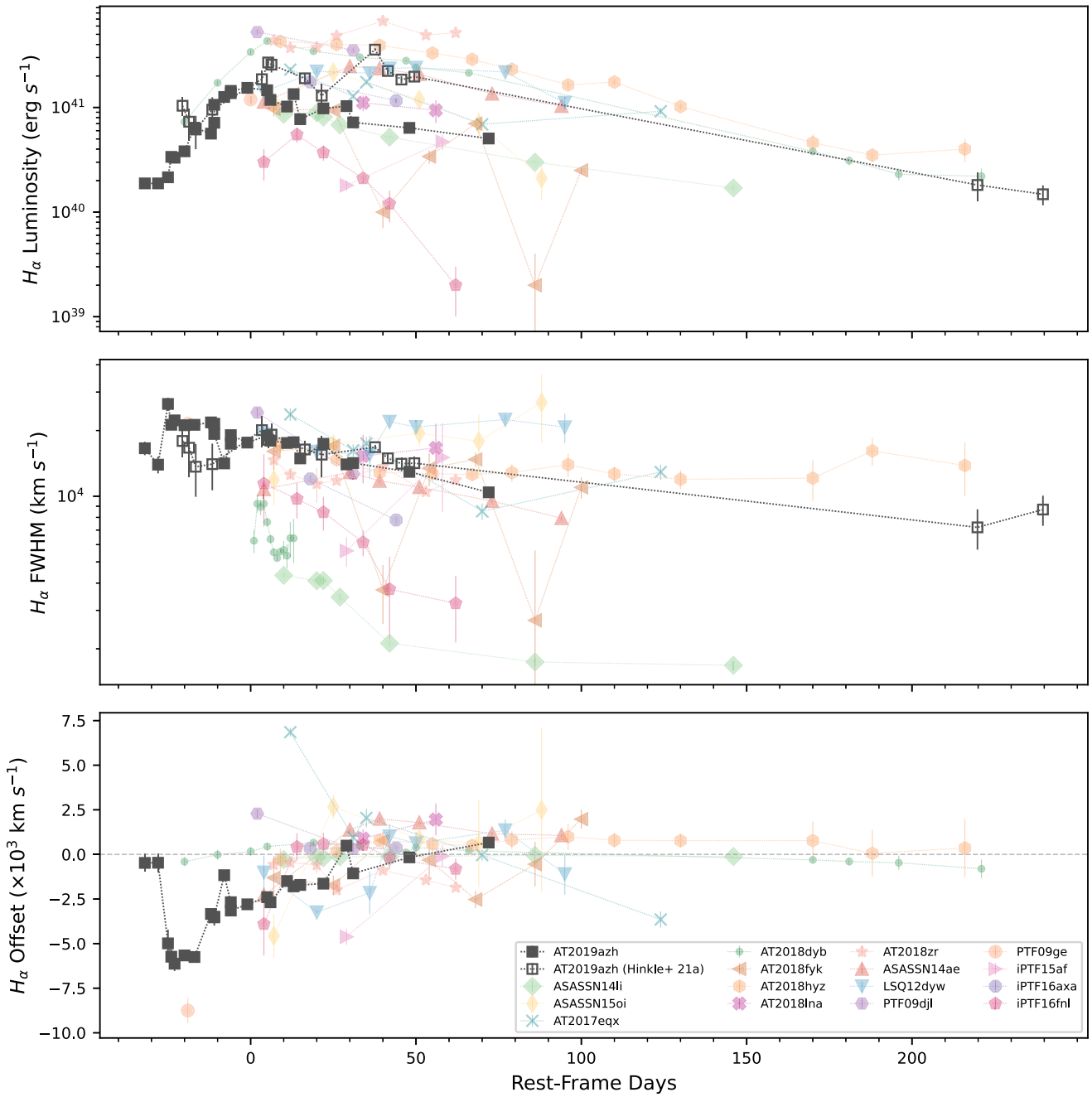

Figure 7. Evolution of Hα line luminosity (top), FWHM (center), and central wavelength offset (bottom) of AT 2019azh from this work compared to those of Hinkle et al. (2021a) and a sample of 15 TDEs from Charalampopoulos et al. (2022). AT 2019azh is plotted relative to its *g*-band peak, while the comparison data are plotted relative to their peak or discovery date (see Charalampopoulos et al. 2022, for details).

(The data used to create this figure are available.)

oversubtraction of the host galaxy spectrum (as they also appear in the SDSS host spectrum as narrow absorption lines; see Figure 2). We also find a strong, narrow [O III] λ5007 absorption line in the host-subtracted spectra (see Figure E1 in Appendix E), which is probably also an oversubtracted host galaxy emission line.

3.2.3. Hα Line Evolution

Following Charalampopoulos et al. (2022), we quantify the evolution of the Hα emission line, as it is a relatively isolated line. For each host- and continuum-subtracted spectrum, we fit the Hα emission line with a Gaussian using the nonlinear least-squares method of the `LMFIT`[59] package. We use the same initial guesses for the center (6563 Å) and width (150 Å, corresponding to a Doppler velocity of ∼10,000 km s^{-1}), for all spectra. All Gaussian fits, after normalizing the peak of the feature, are shown in Figure E3 in Appendix E.

The evolution of the Hα line luminosity is presented in the top panel of Figure 7, along with data from 15 other TDEs obtained from Charalampopoulos et al. (2022), which were measured using

[59] https://lmfit.github.io/lmfit-py/

Table 6
Hα Luminosity, FWHM, and Central Wavelength Offset of AT 2019azh

Phase	Hα Luminosity (10^{40} erg s^{-1})	Hα FWHM (km s^{-1})	Hα Central Wavelength Offset (km s^{-1})
−32	1.88 ± 0.17	16589.22 ± 1171.02	−475.83 ± 487.42
−28	1.88 ± 0.21	13954.00 ± 1231.55	−466.12 ± 522.95
−25	2.15 ± 0.18	26471.07 ± 1809.76	−4986.51 ± 768.48
−24	3.37 ± 0.21	21255.54 ± 1000.60	−5735.38 ± 424.88
−23	3.31 ± 0.19	22257.40 ± 963.45	−6126.03 ± 409.11
−20	3.81 ± 0.14	21156.45 ± 584.78	−5662.58 ± 248.32
−17	6.40 ± 0.28	21238.53 ± 717.22	−5751.50 ± 304.55
−12	5.62 ± 0.23	21790.47 ± 693.67	−3340.03 ± 294.55
−11	7.14 ± 0.46	21490.06 ± 1090.57	−3528.82 ± 463.09
−11	10.59 ± 0.23	19292.27 ± 319.33	−3488.98 ± 135.60
−8	12.63 ± 0.16	14136.78 ± 136.217	−1165.36 ± 57.84
−6	14.45 ± 0.36	17393.32 ± 347.60	−3145.95 ± 147.60
−6	13.69 ± 0.31	19052.18 ± 330.17	−2678.93 ± 140.20
−1	15.43 ± 0.31	17610.98 ± 269.39	−2797.66 ± 114.39
+5	14.56 ± 0.20	18962.47 ± 200.04	−2396.22 ± 84.94
+6	11.84 ± 0.14	17968.18 ± 162.57	−2685.32 ± 69.03
+11	10.18 ± 0.15	17536.29 ± 199.07	−1490.40 ± 84.53
+13	13.39 ± 0.16	17677.46 ± 157.96	−1792.32 ± 67.07
+15	7.72 ± 0.19	14905.48 ± 286.30	−1711.47 ± 121.57
+22	9.80 ± 0.10	17390.90 ± 141.47	−1640.46 ± 60.07
+29	10.26 ± 0.45	13992.84 ± 465.88	491.88 ± 197.83
+31	7.19 ± 0.08	14193.45 ± 124.82	−1065.69 ± 53.00
+48	6.38 ± 0.06	12932.58 ± 95.83	−166.10 ± 40.69
+72	5.05 ± 0.11	10420.17 ± 167.85	664.59 ± 71.28

Note. Phases are given relative to the *g*-band peak brightness.

the same methodology as described here and which constitute the largest sample of homogeneously analyzed TDE spectra to date. Around peak brightness, the Hα luminosity is similar to that of the comparison sample. The post-peak slight decay of the Hα luminosity is also consistent with the rest of the sample. However, the extensive pre-peak spectral observations of AT 2019azh reveal the initial formation of this emission line in a TDE for the first time. These observations can be used to constrain future models of spectral line formation in TDEs. We also compare our results with those of Hinkle et al. (2021a), which agree at early times but not at late times. This might be due to the different analysis method used by Hinkle et al. (2021a), where, for example, the continuum is removed differently than here.

We also measure the evolution of the full width at half-maximum (FWHM) intensity of the Gaussian fits to the Hα emission line of AT 2019azh, and compare them to those of the Charalampopoulos et al. (2022) sample and to the results of Hinkle et al. (2021a) in the middle panel of Figure 7. The FWHM of the Hα emission line of AT 2019azh is at the upper range of the Charalampopoulos et al. (2022) sample, and it shows a clear gradual decline. Here, our results are consistent with those of Hinkle et al. (2021a).

Finally, in the bottom panel of Figure 7, we compare the evolution of the Hα best-fit Gaussian central wavelength offset from the rest wavelength with that of the same sample from Charalampopoulos et al. (2022). While the line centers of the first two spectra are consistent with zero offset, a blueshift rapidly develops and slowly returns back to zero offset within a few months. The magnitude of the offset is consistent with those of other events in the Charalampopoulos et al. (2022) sample, but AT 2019azh is the only event showing this kind of evolution. In addition, from Figure 7, it appears that there is an anticorrelation

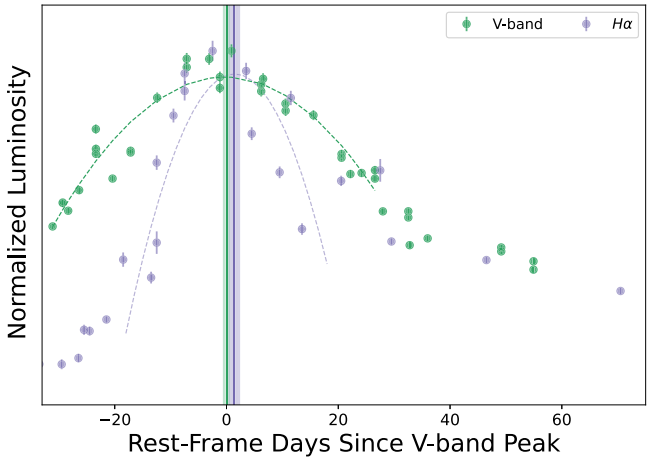

Figure 8. Hα luminosity evolution (purple), compared to the *V*-band light curve of AT 2019azh (green). The colored dashed lines are the parabolic fits to the data around peak brightness, from which the peak times were determined. The vertical solid lines and shaded regions mark the peak times for the *V*-band and Hα peaks, and their 1σ uncertainties, respectively. The Hα peak time is consistent with that of the *V*-band peak.

between the Hα FWHM and offset. Indeed, we find such an anticorrelation (with a Pearson coefficient of −0.876; see Figure E4 in Appendix E). However, events in the Charalampopoulos et al. (2022) sample do not show similar behavior, therefore this anticorrelation does not seem like a universal property of TDEs.

The Hα luminosity, FWHM, and central wavelength offset values for AT 2019azh are presented in Table 6.

Charalampopoulos et al. (2022) showed that TDEs exhibit a time lag between their light curve (i.e., continuum emission) and Hα luminosity peaks. Figure 8 compares the evolution of the Hα luminosity and the *V*-band light curve for AT 2019azh. To determine the peak time of the Hα line luminosity for AT 2019azh, we fit a second-order polynomial to the Hα luminosity from −18 to +18 days since the *g*-band peak and find that the peak occurred on MJD 58569.59 ± 1.07, or $\Delta t = 1.40 \pm 0.93$ days after the *V*-band light-curve peak.

4. Discussion

4.1. Spectroscopic Classification of AT 2019azh

In Figure 9 we compare the continuum-subtracted spectra around the peak of AT 2019azh to those of the Bowen TDE AT 2018dyb (Leloudas et al. 2019), the H+He-TDE AT 2020wey (Charalampopoulos et al. 2023), which also showed a possible early light-curve bump, and AT 2019ahk (Holoien et al. 2019b), which does not show such structure despite having a very densely sampled early-time light curve (see below).[60] AT 2019azh does not show N III λλ4100, 4640 emission like those seen in AT 2018dyb, meaning it is not a Bowen TDE. Its broad H and He II λ4686 emission features are similar to those of AT 2020wey, making it a H+He-TDE. AT 2019ahk shows strong AGN-like narrow spectral emission lines, not seen in most TDEs, implying it might be a different type of flare.

4.2. Peak Luminosity Time Delays

In Section 3.1.1, we measured a time delay in the peak luminosity between the different bands, with the redder bands

[60] We subtract the continuum of each spectrum following the procedure detailed in Section 3.2.2.

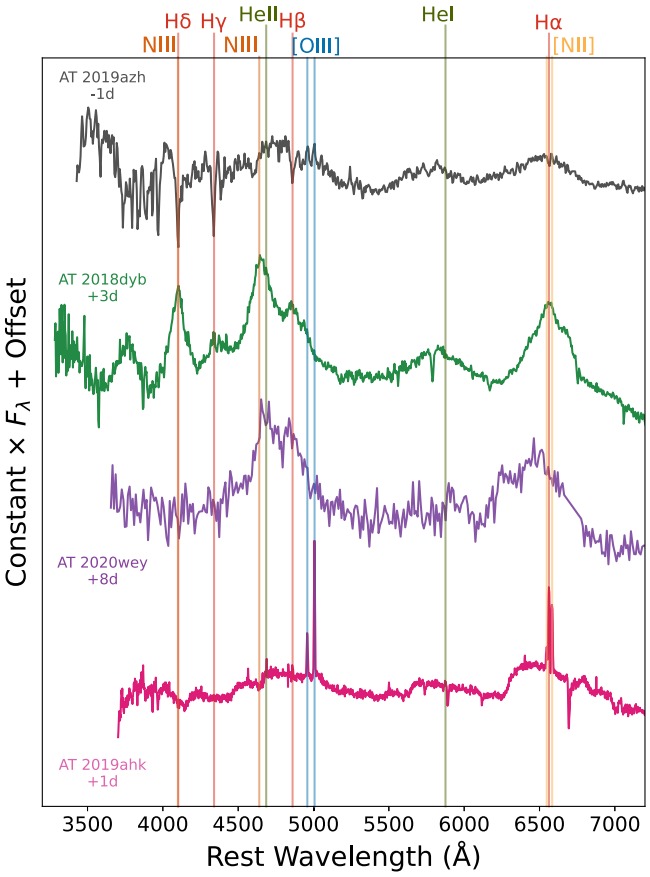

Figure 9. Spectral comparison around peak luminosity of AT 2019azh (host-subtracted spectrum) with the well-observed Bowen TDE AT 2018dyb (Leloudas et al. 2019, not host subtracted), the H+He-TDE AT 2020wey (Charalampopoulos et al. 2023, host subtracted), which also showed possible early light-curve structure, and AT 2019ahk (Holoien et al. 2019b, not host subtracted), which did not show such structure in its very densely sampled light-curve rise. All spectra are continuum-subtracted. The similarity of the AT 2019azh spectrum to that of AT 2020wey classifies it as a H+He-TDE. The spectrum of AT 2019ahk displays distinctive narrow emission lines, implying it might be an AGN-related flare rather than a *classical* TDE. Days relative to the light-curve peak are shown next to each spectrum.

peaking later than the bluer ones (Figure 3). Such behavior has been seen in other TDEs, such as AT 2018zr (PS18kh; Holoien et al. 2019a), AT 2019ahk (ASASSN-19bt; Holoien et al. 2019b), and AT 2018dyb (ASASSN-18pg; Holoien et al. 2020), where it has been attributed to the blackbody temperature evolution around the peak. Wang et al. (2023) also find that the optical emission lags behind the UV emission in the peculiar nuclear transient AT 2019avd. They interpret this lag as evidence for the optical emission being reprocessed UV emission. This phenomenon is also observed in AGNs (e.g., Shappee et al. 2014), where it is attributed to an accretion disk emission model (e.g., Cackett et al. 2007), according to which the inner, hotter accretion disk is illuminated by X-rays first, with the illumination progressing outward, causing variations in the light curve to manifest initially in the bluer bands associated with the inner disk, followed by the redder bands. An opposite time delay was measured for the TDE ASASSN-14li by Pasham et al. (2017). There, the UV lagging behind the optical is interpreted as evidence for the stream collision scenario.

4.3. Early Light-curve Structure

Our high-cadence photometric observations also reveal, for the first time, both a change in light-curve slope and a possible bump in the rising light curve of a TDE. The most densely sampled rising light curve of a TDE is that of AT 2019ahk (ASASSN-19bt; Holoien et al. 2019b), which was observed with a 30 minute cadence using TESS. Its light-curve rise is smooth (Figure 10), in stark contrast to that of AT 2019azh. However, AT 2019ahk might not be a spectroscopically *classical* TDE. As mentioned, it stands out in Figure 9 owing to its strong and narrow [O III] $\lambda\lambda$4959, 5007 and [N II] $\lambda\lambda$6548, 6584 emission lines, not commonly seen in TDE spectra. Furthermore, the host galaxy of AT 2019ahk is in the Seyfert region of the Baldwin–Phillips–Terlevich (Baldwin et al. 1981) diagram (see Figure 2 in Holoien et al. 2019b), indicating the presence of an AGN as an ionizing source. AT 2019ahk might thus be related to an AGN flare rather than a typical optical/UV TDE.

ASASSN-14ko (Holoien et al. 2014a) is another nuclear transient with a bump reported in its rising phase (Huang et al. 2023). However, it displays spectra more similar to those of AGNs (Payne et al. 2021) and periodicity in its outbursts (Payne et al. 2021, 2022, 2023), which are not seen in the class of TDEs to which AT 2019azh belongs. Hence, we do not consider it further here.

AT 2020wey, on the other hand, is a classical spectroscopically classified TDE (Figure 9), which does show a possible bump in its early *g*- and *r*-band light curves (Figure 10; Charalampopoulos et al. 2023). Unfortunately, this part of the light curve of AT 2020wey was not observed at a sufficiently high cadence to robustly characterize this feature. Finally, AT 2020zso is a TDE, which shows an abrupt change in its light-curve rise slope (Figure 10; photometry taken from Wevers et al. 2022).

No TDE emission model predicts specific light-curve features such as these. This could point toward the presence of more than one emission source as responsible for the UV/optical TDE emission. The photometry presented here could be used to test future TDE emission models.

4.4. Estimates of the SMBH Mass

Wevers (2020) derived the SMBH mass of the host of AT 2019azh using the M–σ relation from Gültekin et al. (2009a) with the velocity dispersion measured from the WHT spectrum presented here. They find an SMBH mass of $M_{\rm BH} = 2.29 \pm 2.27 \times 10^6\,M_\odot$. This mass is consistent with that found by `TDEMass` but is a factor of $\sim$7 smaller than that found by `MOSFiT`. We do not consider this definitive evidence favoring one model or the other since the host-galaxy-derived SMBH mass strongly depends on the choice of scaling relation and the spectral resolution used to infer the velocity dispersion, as is evident in the comparison to other works.

We present a summary of SMBH mass estimates obtained here and in other works using the two light-curve models and host galaxy scaling relations, along with the corresponding Eddington ratios for the peak bolometric luminosity, in Table 7. Our results are consistent with those of Hammerstein et al. (2023) for the `TDEMass` estimates, and marginally consistent (at the $\lesssim 2\sigma$ level) with the MOSFiT estimates from that work. Our results are not consistent with those of Hinkle et al. (2021a) or Nicholl et al. (2022). The discrepancy with

Table 7
SMBH Mass Estimates and Corresponding Eddington Ratios for the Peak Bolometric Luminosity

References	TDEMass		MOSFiT		Host Galaxy	
	$M_{\rm BH}$ ($10^6\,M_\odot$)	$L_{\rm bol}/L_{\rm Edd}$	$M_{\rm BH}$ ($10^6\,M_\odot$)	$L_{\rm bol}/L_{\rm Edd}$	$M_{\rm BH}$ ($10^6\,M_\odot$)	$L_{\rm bol}/L_{\rm Edd}$
This work	$2.50^{+0.29}_{-0.24}$	$0.78^{+0.22}_{-0.21}$	$16.22^{+0.75}_{-0.75}$	$0.12^{+0.03}_{-0.03}$	2.29 ± 2.27[a]	0.85 ± 0.87
Hammerstein et al. (2023)	$2.19^{+0.14}_{-0.00}$	$0.85^{+0.18}_{-0.03}$	$26.91^{+6.81}_{-5.30}$	$0.07^{+0.02}_{-0.02}$	…	…
Hinkle et al. (2021a)	$0.73^{+0.24}_{-0.10}$	$6.75^{+2.23}_{-0.95}$	$7.8^{+3.9}_{-4.1}$	$0.63^{+0.32}_{-0.33}$	~12.59[b]	~0.34
Liu et al. (2022)	…	…	…	…	$23.0^{+13.0}_{-12.0}$[c]	~0.06
Nicholl et al. (2022)	…	…	$5.01^{+0.70}_{-0.81}$	…	…	…

Notes. Eddington ratios are calculated for each source using their respective SMBH masses and peak bolometric luminosities.
[a] Value from Wevers (2020) using the WHT spectrum presented here and the Gültekin et al. (2009b) scaling relation.
[b] Using the SDSS DR14 spectrum and the Gültekin et al. (2009b) scaling relation.
[c] Using the Reines & Volonteri (2015) scaling relation.

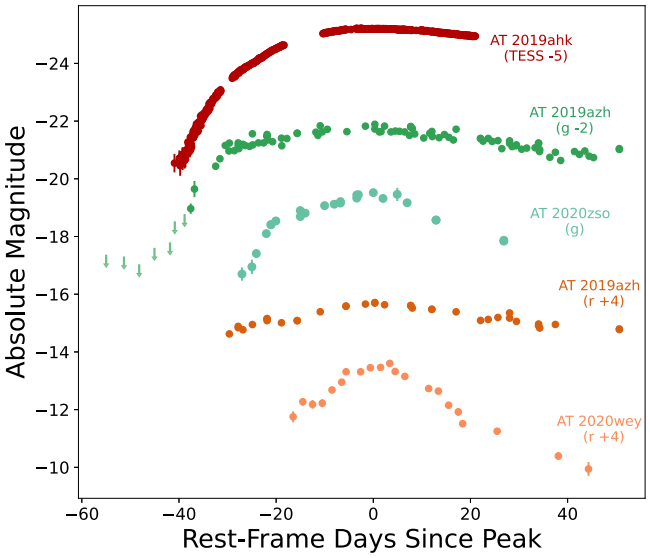

Figure 10. Comparison between the light curves of AT 2019azh (ASAS-SN and Las Cumbres data only, shown for clarity) to those of AT 2019ahk, the TDE with the most densely sampled light curve to date (Holoien et al. 2019b), AT 2020wey (Charalampopoulos et al. 2023), and AT 2020zso. AT 2019ahk lacks any pronounced early-time light-curve structure like that seen in AT 2019azh, despite having high-cadence TESS observations. In contrast, the light curve of the TDE AT 2020wey shows a possible early bump in its *r*-band light curve, and AT 2020zso exhibits a change in its rising slope. Arrows indicate 3σ nondetection upper limits.

Hinkle et al. (2021a) could be due to their use of the pre-corrected UVOT calibrations introduced later by Hinkle et al. (2021b).

4.5. Estimates of the Disrupted Star Mass

The mass derived for the disrupted star also differs substantially between the models, with TDEMass preferring a star roughly 1 order of magnitude more massive than MOSFiT ($4.8^{+4}_{-2.5}$ versus $0.10^{+0.02}_{-0.03}$ $M_\odot$, respectively). In addition to the different model assumptions, this difference could be driven by the MOSFiT prior of a Kroupa initial mass function. Hinkle et al. (2021a) find a similar stellar mass in their MOSFiT fit as in ours, but a much higher one in their TDEMass fit than ours. As mentioned previously, this comparison may not be entirely accurate because of the Swift calibration updates (Hinkle et al. 2021b), not available to Hinkle et al. (2021a), which could influence their bolometric luminosity calculations. Hammerstein et al. (2023) also estimated the stellar mass using these two methods. Our TDEMass-based stellar mass is consistent with their findings, while our MOSFiT-based stellar mass is not. This might be due to differences in the priors used for the efficiency parameter, which is degenerate with the stellar mass. The efficiency parameter inferred from MOSFiT in our analysis is close to the maximum limit of the prior (see Figure C1 in Appendix C). This relatively high efficiency might be additional evidence for contributions to the emission from the stream collision process.

4.6. Self-consistency of MOSFiT Parameters

For the best-fit stellar mass of 0.1 $M_\odot$ and BH mass of $10^{7.21}$ $M_\odot$ given by MOSFiT (see Table 5), assuming $R_\star \approx R_\odot(M_\star/M_\odot) \approx 0.1R_\odot$ (Demircan & Kahraman 1991), the canonical tidal radius is $R_{\rm t} \approx R_\star(M_{\rm BH}/M_\star)^{1/3} \approx 1.6\,GM_{\rm BH}/c^2$. In order to be tidally disrupted and not directly captured by the BH, the tidal radius must be outside of the direct-capture radius (which is larger than the horizon radius for all BH spins $a < 1$, and is $4GM/c^2$ for $a = 0$; e.g., Will 2012). The direct-capture radius is a function of the BH spin, the square of the specific angular momentum of the star, and the projection of the angular momentum onto the spin axis of the BH, and is minimized at a value of[61] $R_{\rm dc} = GM/c^2(1 + \sqrt{1-a})^2$. Requiring that $R_{\rm t} \geqslant R_{\rm dc}$ here sets $a \gtrsim 0.93$ for *any* star to be tidally disrupted and not directly captured. In fact, even with a spin value of $a \approx 1$, it is statistically improbable for the star to be injected into the loss cone, tidally disrupted, and not directly captured; if we assume that stars entering the loss cone are isotropically distributed at large radii and we are in the pinhole regime, such that two-body interactions result in a large relative change in the square of the specific angular momentum of the star on a per orbit basis (e.g., Frank & Rees 1976; Lightman & Shapiro 1977; Merritt 2013; Stone & Metzger 2016), then the formalism described by Coughlin & Nixon (2022) predicts for the parameters here that the fraction of TDEs (i.e., the fraction of stars injected into the loss cone that are tidally disrupted and not directly captured) is ~0.6%. This makes the result highly unlikely.

If the event were a partial TDE, these spin constraints and low probabilities would be somewhat ameliorated. Since a partial TDE occurs at $\sim 2r_{\rm t}$ for a low-mass star (Guillochon & Ramirez-Ruiz 2013; Mainetti et al. 2017; Miles et al. 2020; see

[61] We assume $a > 0$ in this expression, i.e., the stellar angular momentum is aligned with the BH spin (e.g., Will 2012; D'Orazio et al. 2019; Coughlin & Nixon 2022).

also Gafton et al. 2015 in the relativistic case at a comparable BH mass, in particular their Figure 3), the corresponding limit on the BH spin is $a \gtrsim 0.39$. The probability of being tidally disrupted and not directly captured for a BH spin of $a = 0.999$ is then ∼5.1%. Additionally, Coughlin & Nixon (2019) and Miles et al. (2020) found that the fallback rate asymptotically declines as $\propto t^{-9/4}$ (rather than the canonical $t^{-5/3}$) in the case of a partial TDE, which is also more consistent with the best-fit power law of $t^{-2.05}$ for AT 2019azh (assuming that the fallback rate closely tracks the accretion luminosity (e.g., Mockler et al. 2019; Nicholl et al. 2022). However, `MOSFiT` finds a best-fit scaled impact parameter of $b = 0.99^{+0.01}_{-0.03}$, indicating a full disruption. This means that the best-fit $M_{\rm BH}$, $M_\star$, and b from `MOSFiT` are not self-consistent with a fully accretion-powered picture.

Using the extreme upper and lower values for $M_\star$ and $M_{\rm BH}$, respectively, allowed by the total errors listed in Table 5 amealiorates the problem, requiring $a \gtrsim 0.14$ for a full disruption. In addition, if some of the early emission is contributed by outer shocks, this would decrease the rise-time of the accretion-powered part of the light curve, reducing $M_{\rm BH}$ even further, and making a full disruption more likely. We conclude that `MOSFiT` can only marginally fit the data self-consistently assuming a fully accretion-powered light curve, and that at least some contribution from an additional power source at early times is necessary.

If we perform the same calculations using the values from `TDEMass` (i.e., $M_{\rm BH} = 2.5^{+0.29}_{-0.24} \times 10^6\ M_\odot$, $M_\star = 4.8^{+4}_{-2.5}\ M_\odot$), where in this case $R_\star \approx 3R_\odot$ (Demircan & Kahraman 1991), we find $R_{\rm t} \approx 44.3\, GM_{\rm BH}/c^2$. Here, $R_{\rm t} \geqslant R_{\rm dc}$ for any black hole (BH) spin, making this model entirely self-consistent.

4.7. Time Lag between Hα Emission and the Continuum

Our time lag of 1.40 ± 0.93 days between the V-band light curve and Hα luminosity is inconsistent with that of Hinkle et al. (2021a) who measure a ∼23 days time lag. This stems mainly from a difference between our determination of the light-curve peak and theirs. Their light-curve peak was measured at MJD $58548^{+6.30}_{-2.60}$ (roughly 19 days before ours). This peak was determined by Hinkle et al. (2021a) as the median value obtained from fitting a second-order polynomial to 10,000 realizations of bolometric light curves, generated from bolometrically corrected ASAS-SN g-band data, with the bolometric corrections inferred from blackbody fits. The peak light-curve time determined by Hammerstein et al. (2023) of MJD $58566^{+1.16}_{-1.75}$ is closer to ours.

5. Summary and Conclusions

AT 2019azh is a H+He-TDE and is one of the best-observed UV/optical TDEs to date, having extensive spectroscopic coverage and multiwavelength photometric coverage starting several weeks before peak brightness (Figure 1). These observations reveal the following for the first time:

1. A robust change in slope and possible bump in the early light curve of a TDE.
2. The early evolution of the Hα emission line in a TDE.

Unfortunately, no models exist today that can be compared to these observational characteristics; however, they could be used to constrain future models of TDE emission sources and line formation. Relatively high cadence (1–2 days) observations of TDEs are required to test if the light-curve structure observed in AT 2019azh is a common feature of rising TDE light curves.

We detect a possible MIR excess beyond what is expected from the optical/UV blackbody at those wavelengths. This excess, detected 5.15 days after the g-band peak, might be due to a prompt dust echo. However, we are not able to determine its origin without additional observations.

The post-peak bolometric decline of AT 2019azh is not well described by a $t^{-5/3}$ power law, or by any power law, but is better fit by an exponential. We find no significant delay between the peak of the V-band light curve and the Hα luminosity in AT 2019azh.

High-cadence pre-peak observations of more TDEs will be able to determine how common the features seen here are among the TDE population. In addition, more detailed modeling of TDE emission is needed to match the quality of current TDE observations and to help constrain the emission mechanism(s) in TDEs. This is an essential step before we can use TDEs to robustly measure SMBH properties.

Acknowledgments

We thank B. Mockler for helpful advice on using MOSFiT. S.F., I.A., and L.M. acknowledge support from the European Research Council (ERC) under the European Union's Horizon 2020 research and innovation program (grant agreement No. 852097). S.F. and I.A. acknowledge further support from the Israel Science Foundation (grant No. 2108/18). The Las Cumbres Observatory group is supported by National Science Foundation (NSF) grants AST-1911225 and AST-1911151. P.C. and O.G. were supported by the Science & Technology Facilities Council (grants ST/S000550/1 and ST/W001225/1). G.L. was supported by a research grant (19054) from VILLUM FONDEN. M.N. is supported by the ERC under the European Union's Horizon 2020 research and innovation program (grant agreement No. 948381) and by UK Space Agency grant No. ST/Y000692/1. C.P.G. acknowledges financial support from the Secretary of Universities and Research (Government of Catalonia) and by the Horizon 2020 Research and Innovation Program of the European Union under the Marie Skłodowska-Curie program. The SNICE research group acknowledges financial support from the Spanish Ministerio de Ciencia e Innovación (MCIN), the Agencia Estatal de Investigación (AEI) 10.13039/501100011033, and the European Social Fund (ESF) "Investing in your future" under the 2019 Ramón y Cajal program RYC2019-027683-I and the PID2020-115253GA-I00 HOSTFLOWS project, from Centro Superior de Investigaciones Científicas (CSIC) under the PIE project 20215AT016, and the program Unidad de Excelencia María de Maeztu CEX2020-001058-M, and from the Departament de Recerca i Universitats de la Generalitat de Catalunya through the 2021-SGR-01270 grant. S.M. and T.R. acknowledge support from the Research Council of Finland project 350458. A.V.F.'s group at UC Berkeley has been supported by the Christopher R. Redlich Fund, William Draper, Timothy and Melissa Draper, Briggs and Kathleen Wood, Sanford Robertson (T.G.B. is a Draper-Wood-Robertson Specialist in Astronomy), and numerous other donors. F.O. acknowledges support from MIUR, PRIN 2020 (grant 2020KB33TP) "Multimessenger astronomy in the Einstein Telescope Era (METE)." E.R.C. acknowledges support from the National Science Foundation through grant AST-2006684. P.C. acknowledges support via an Academy of

Finland grant (340613; PI: R. Kotak). This work was funded in part by ANID, Millennium Science Initiative, ICN12_009.

This work is based in part on observations collected at the Las Cumbres Observatory, the Copernico 1.82 m Telescope (Asiago Mount Ekar, Italy) operated by the Italian National Astrophysical Institute—INAF, Osservatorio Astronomico di Padova, the European Organization for Astronomical Research in the Southern Hemisphere, Chile, as part of ePESSTO under ESO program ID 199.D-0143(T) (PIs: S. Smartt, C. Inserra), the Nordic Optical Telescope, owned in collaboration by the University of Turku and Aarhus University, and operated jointly by Aarhus University, the University of Turku, and the University of Oslo, representing Denmark, Finland, and Norway, the University of Iceland and Stockholm University at the Observatorio del Roque de los Muchachos, La Palma, Spain, of the Instituto de Astrofisica de Canarias, and on observations made under programme W/2019B/P7 with the William Herschel Telescope operated on the island of La Palma by the Isaac Newton Group of Telescopes in the Spanish Observatorio del Roque de los Muchachos of the Instituto de Astrofísica de Canarias. The NOT observations were obtained through the NUTS Collaboration supported in part by the Instrument Center for Danish Astrophysics (IDA). A major upgrade of the Kast spectrograph on the Shane 3 m telescope at Lick Observatory was made possible through generous gifts from William and Marina Kast as well as the Heising-Simons Foundation. Research at Lick Observatory is partially supported by a generous gift from Google. We thank for their assistance the staff at the various observatories where data were obtained.

This research has made use of the NASA/IPAC Infrared Science Archive, which is funded by the National Aeronautics and Space Administration (NASA) and operated by the California Institute of Technology. This publication also makes use of data products from NEOWISE, which is a project of the Jet Propulsion Laboratory/California Institute of Technology, funded by the Planetary Science Division of NASA. This publication makes use of data products from the WISE, which is a joint project of the University of California, Los Angeles, and the Jet Propulsion Laboratory/California Institute of Technology, funded by NASA.

Supporting research data are available on reasonable request from the corresponding author.

Appendix A
MIR Light Curve

Figure A1 displays the MIR light curves of AT 2019azh. A significant MIR flare appears at 5.15 days after the *g*-band peak.

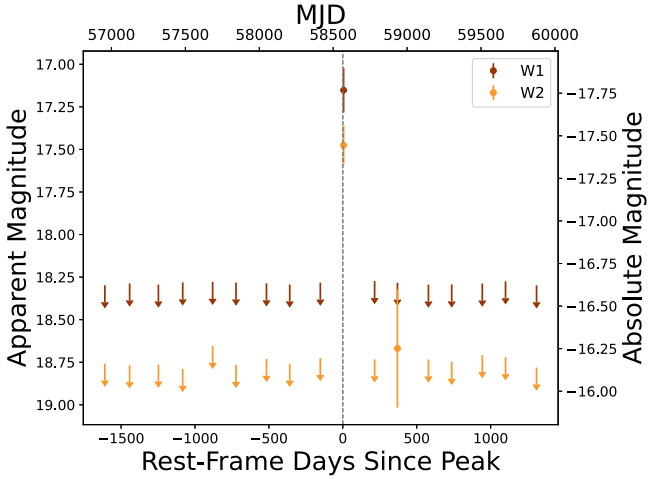

Figure A1. Milky Way extinction-corrected MIR light curves of AT 2019azh from WISE in days relative to the *g*-band peak. Arrows indicate 3σ nondetection upper limits and the dashed vertical line indicates the *g*-band peak.

Appendix B
UV/Optical Peak Fits

Figure B1 displays the second-order polynomial fits around the peak of the light curve for different bands.

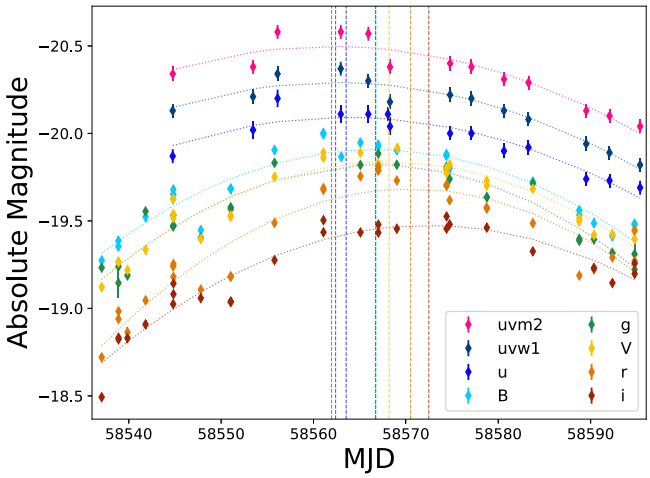

Figure B1. Parabolic fits of the host-subtracted Las Cumbres optical photometry and Swift UV photometry of AT 2019azh around peak brightness. The dashed vertical lines indicate the time of peak for each band from the best-fit parabola.

Appendix C
MOSFiT Best-fit Parameters

Figure C1 shows the two-dimensional MOSFiT posterior parameters distributions. The model fit can be seen to be well converged.

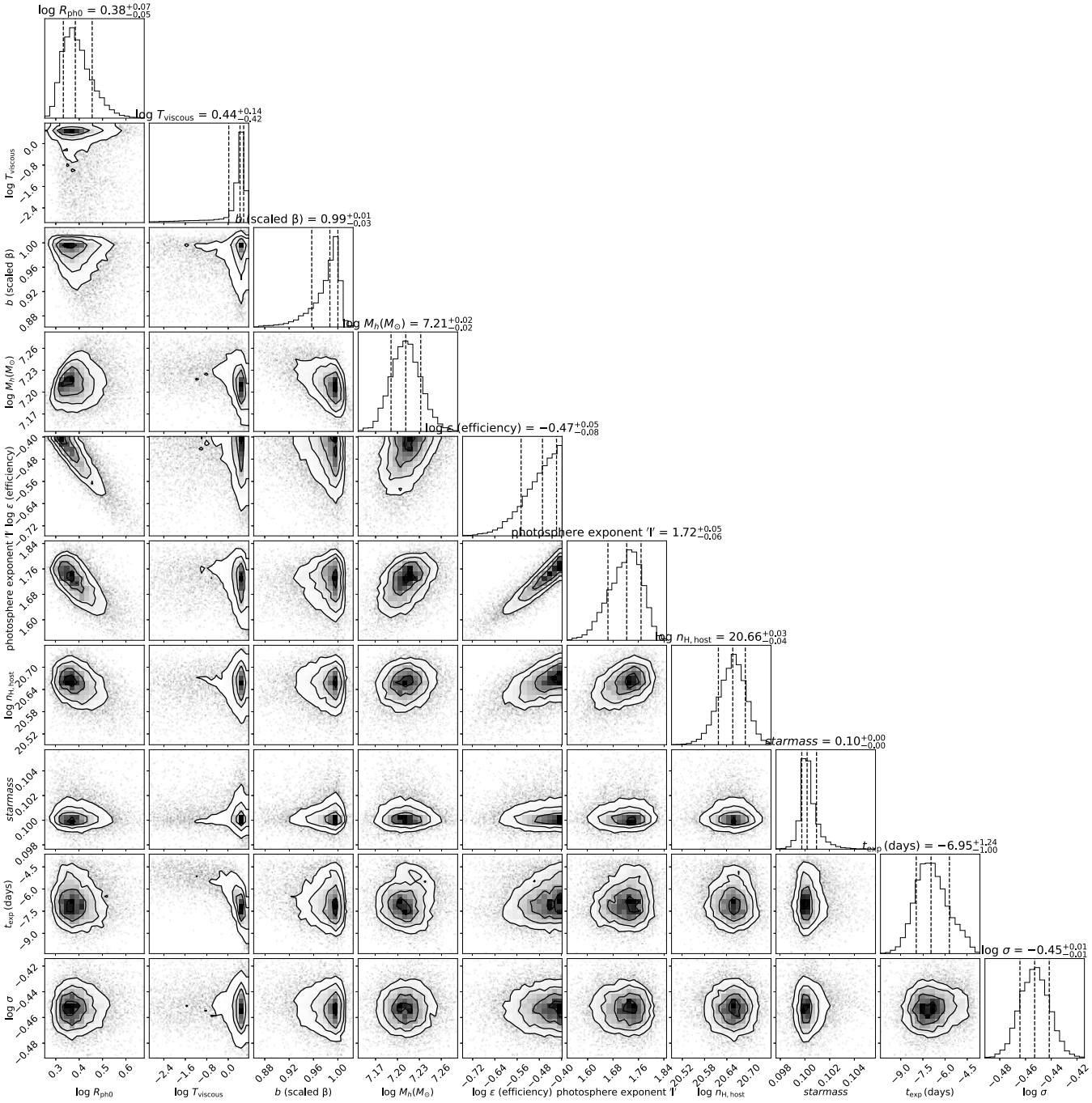

Figure C1. Corner plot showing the posterior parameter distributions for the MOSFiT model fit. 1σ confidence intervals are marked.

Appendix D
TDEMass Parameters

Figure D1 shows the inferred SMBH and star masses from TDEMass, based on the peak bolometric luminosity and the blackbody temperature at the peak from SuperBol.

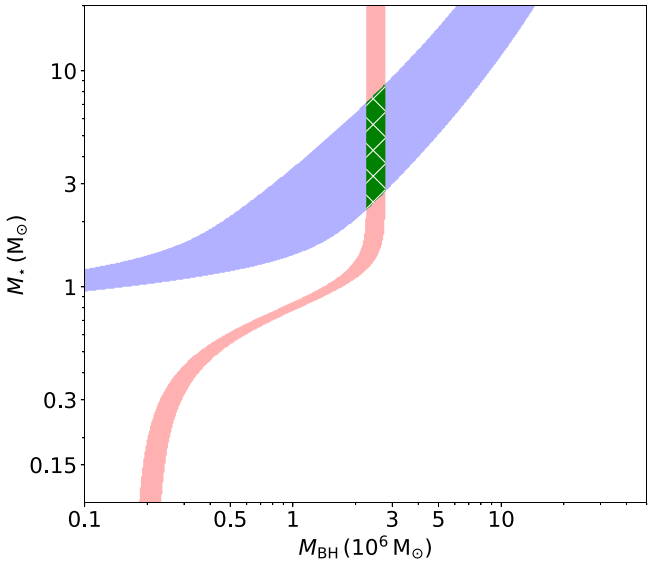

Figure D1. Inferred BH and star masses from TDEMass, with the blue shaded region indicating the range of solutions for the peak bolometric luminosity, and the red shaded region indicating the range of solutions for the blackbody temperature at this peak. The green region indicates the overlapping solutions.

Appendix E
Spectral Data Processing

Figure E1 displays the step-by-step data-processing procedure applied on a spectrum obtained 13 days after the light-curve peak, as outlined in Section 3. The same procedure is applied to all spectra of AT 2019azh, apart from the du Pont and the WHT spectra for the reasons detailed in Section 3.

Figure E2 shows the spectroscopic evolution of AT 2019azh, after photometric calibration, host subtraction, and continuum removal, as described in Section 3.

Figure E3 shows the Gaussian fits of the Hα line performed on the host galaxy and continuum-subtracted spectra. Masking the feature around 6100–6200 Å does not significantly alter the fits, indicating that they are not strongly affected by this feature. In the −32 days spectrum, removing the data blueward of 6200 Å also does not significantly alter the fit, indicating that it is not strongly affected by the emission seen there.

Figure E4 shows the relation between the offset of the Hα line and its FWHM for AT 2019azh. The plot reveals a strong anticorrelation between these two properties.

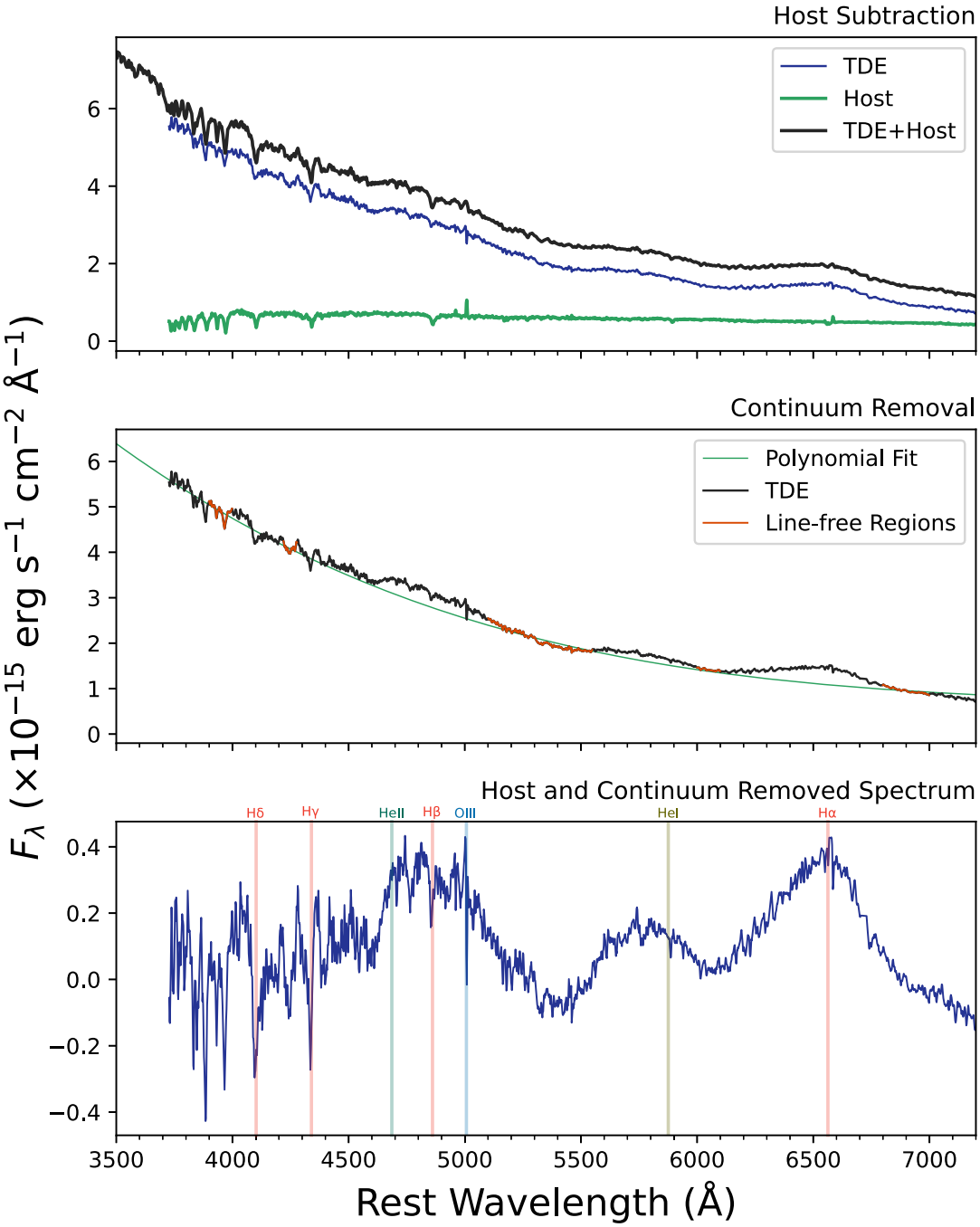

Figure E1. Top: archival resampled SDSS host galaxy spectrum (green), the photometrically calibrated spectrum of AT 2019azh, including host contamination, 13 days after light-curve peak (black), and the host-subtracted TDE spectrum (blue). Middle: host-subtracted spectrum (black) with selected line-free regions (red) used for polynomial fitting (green). Bottom: host and continuum-subtracted spectrum, showing broad Hα, He II λ4686, and He I λ5876 emission lines. The narrow [O III] λ5007 and Balmer lines are likely oversubtracted host galaxy lines.

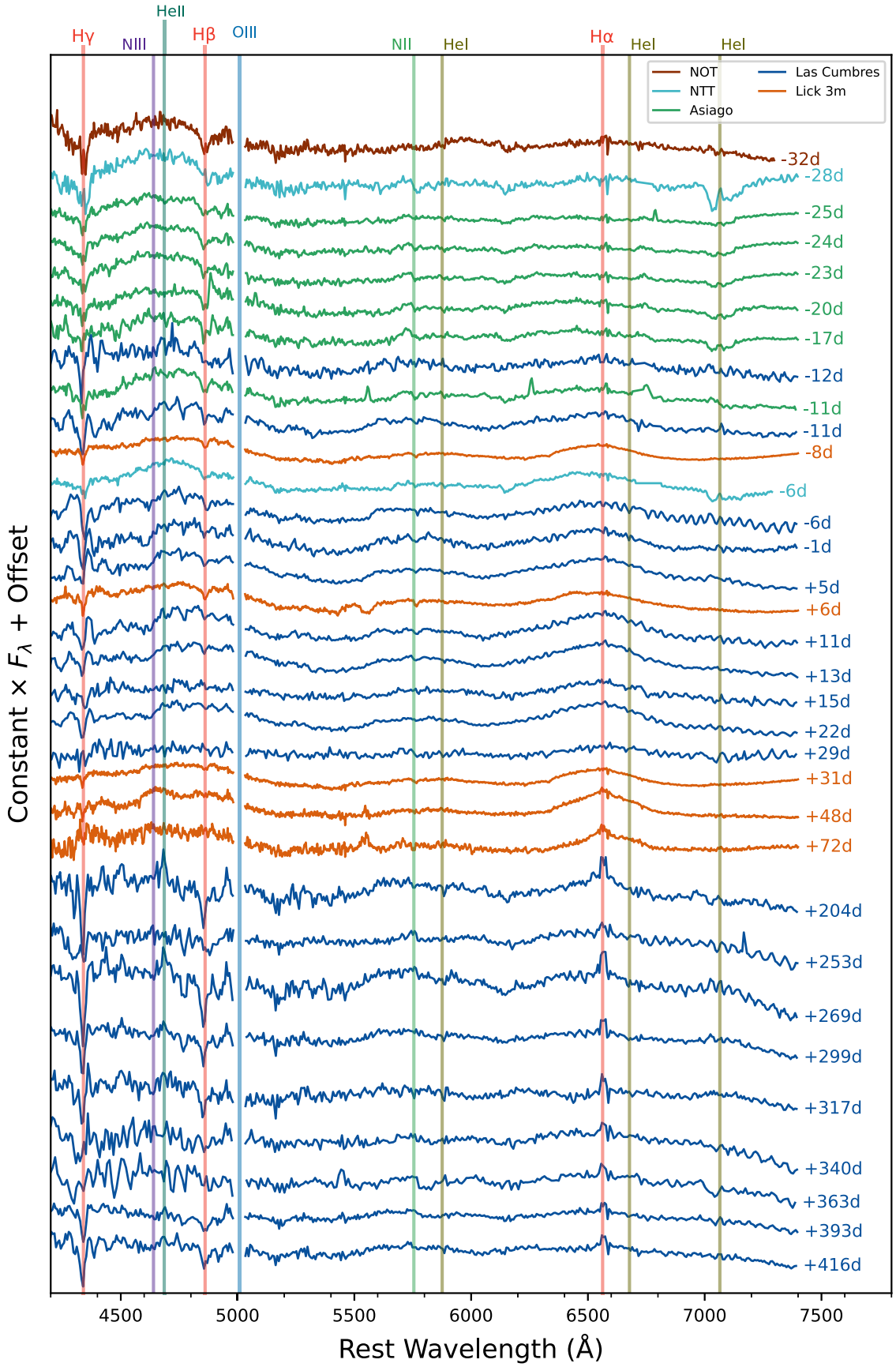

Figure E2. Spectroscopic evolution of AT 2019azh after host galaxy and continuum removal. [O III] λ5007 lines are masked for display purposes. The phase of each spectrum relative to the *g*-band light-curve peak is indicated beside it.

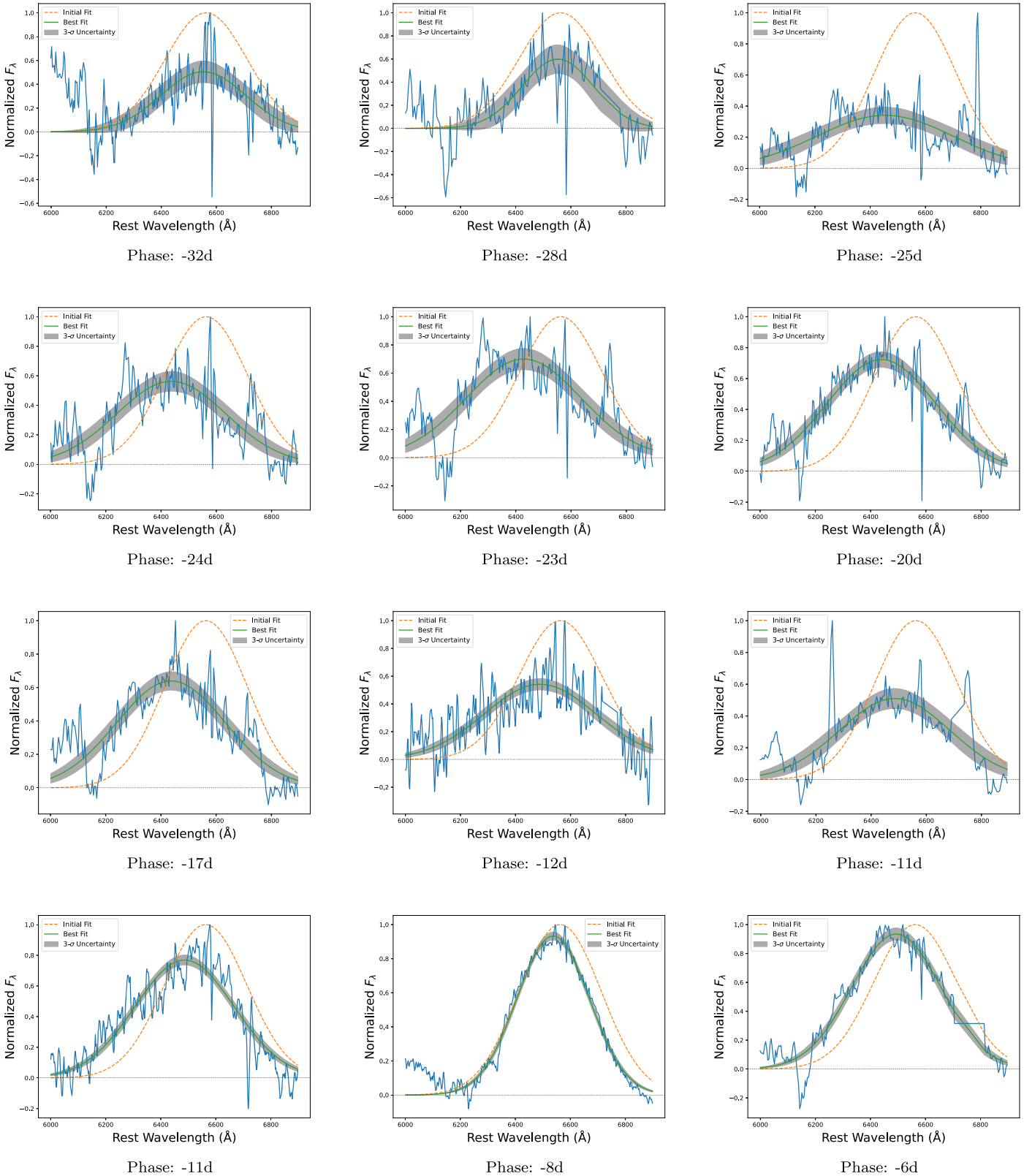

Figure E3. Best-fit results from fitting the Hα line with a Gaussian are shown with solid green lines and the 3σ errors are represented in gray. In each case, the dashed line indicates the initial guess for the fit. Phases are noted in rest-frame days relative to the g-band light-curve peak.

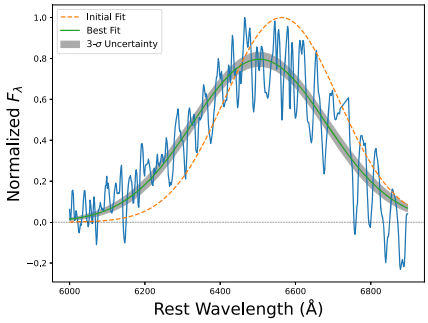

Phase: -6d

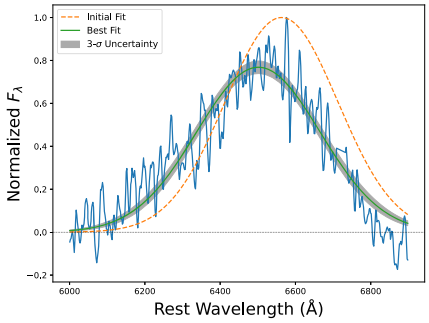

Phase: -1d

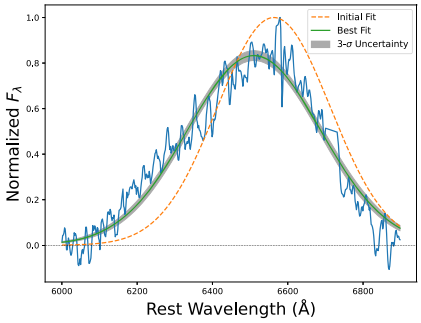

Phase: +5d

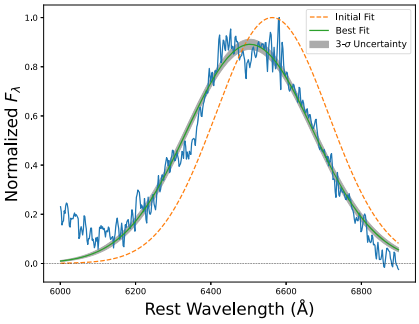

Phase: +6d

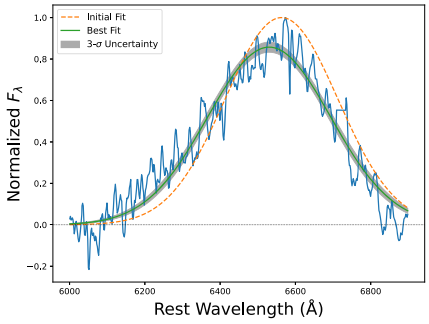

Phase: +11d

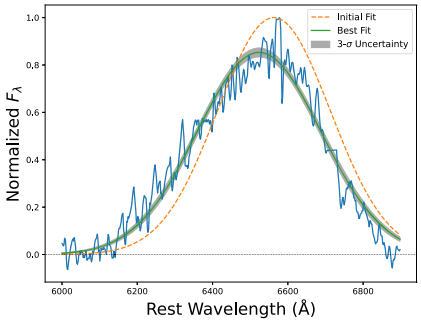

Phase: +13d

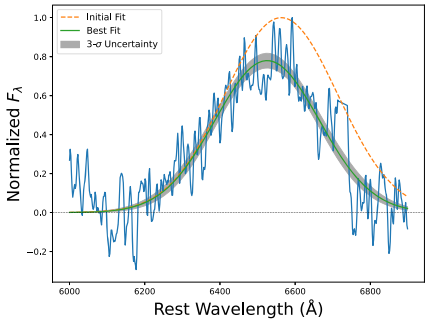

Phase: +15d

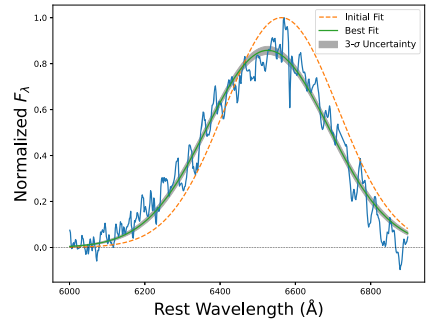

Phase: +22d

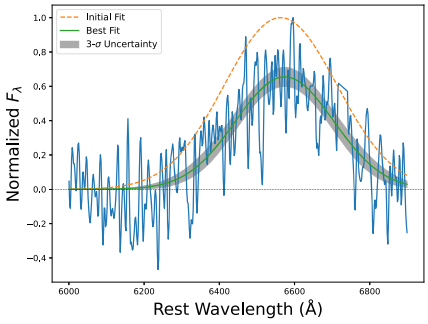

Phase: +29d

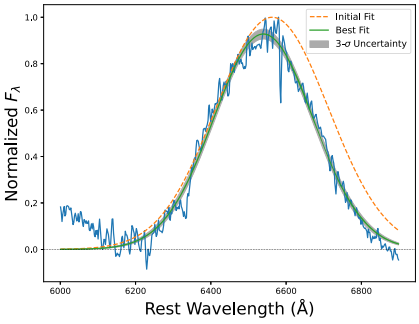

Phase: +31d

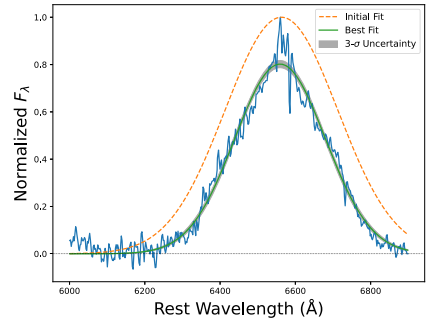

Phase: +48d

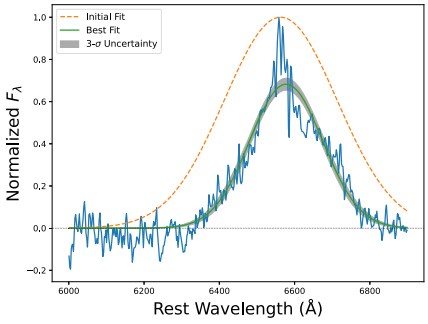

Phase: +72d

Figure E3. (Continued.)

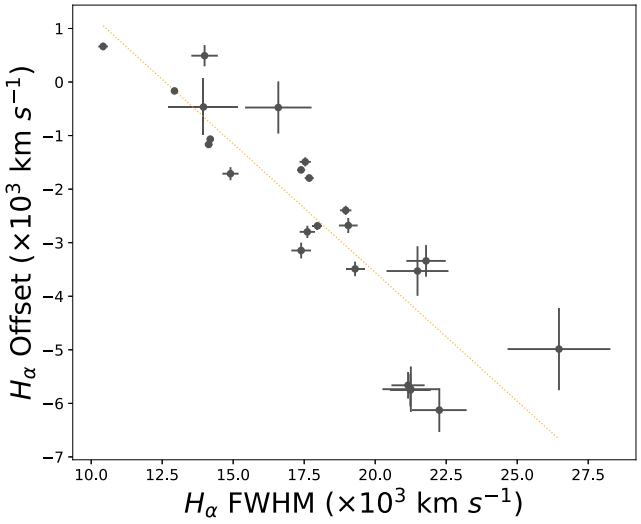

Figure E4. The anticorrelation between the Hα offset and FWHM in AT 2019azh, with a Pearson coefficient of −0.876. A linear fit is shown in the dashed orange line, having a slope of −0.481.

ORCID iDs

Sara Faris https://orcid.org/0009-0007-8485-1281
Iair Arcavi https://orcid.org/0000-0001-7090-4898
Lydia Makrygianni https://orcid.org/0000-0002-7466-4868
Daichi Hiramatsu https://orcid.org/0000-0002-1125-9187
Giacomo Terreran https://orcid.org/0000-0003-0794-5982
Joseph Farah https://orcid.org/0000-0003-4914-5625
D. Andrew Howell https://orcid.org/0000-0003-4253-656X
Curtis McCully https://orcid.org/0000-0001-5807-7893
Megan Newsome https://orcid.org/0000-0001-9570-0584
Estefania Padilla Gonzalez https://orcid.org/0000-0003-0209-9246
Craig Pellegrino https://orcid.org/0000-0002-7472-1279
K. Azalee Bostroem https://orcid.org/0000-0002-4924-444X
Marco C. Lam https://orcid.org/0000-0002-9347-2298
Lina Tomasella https://orcid.org/0000-0002-3697-2616
Thomas G. Brink https://orcid.org/0000-0001-5955-2502
Alexei V. Filippenko https://orcid.org/0000-0003-3460-0103
K. Decker French https://orcid.org/0000-0002-4235-7337
Peter Clark https://orcid.org/0000-0002-6576-7400
Or Graur https://orcid.org/0000-0002-4391-6137
Giorgos Leloudas https://orcid.org/0000-0002-8597-0756
Mariusz Gromadzki https://orcid.org/0000-0002-1650-1518
Joseph P. Anderson https://orcid.org/0000-0003-0227-3451
Matt Nicholl https://orcid.org/0000-0002-2555-3192
Claudia P. Gutiérrez https://orcid.org/0000-0003-2375-2064
Erkki Kankare https://orcid.org/0000-0001-8257-3512
Cosimo Inserra https://orcid.org/0000-0002-3968-4409
Lluís Galbany https://orcid.org/0000-0002-1296-6887
Thomas Reynolds https://orcid.org/0000-0002-1022-6463
Seppo Mattila https://orcid.org/0000-0001-7497-2994
Teppo Heikkilä https://orcid.org/0000-0002-7845-8965
Yanan Wang https://orcid.org/0000-0003-3207-5237
Francesca Onori https://orcid.org/0000-0001-6286-1744
Thomas Wevers https://orcid.org/0000-0002-4043-9400
Eric R. Coughlin https://orcid.org/0000-0003-3765-6401
Panos Charalampopoulos https://orcid.org/0000-0002-0326-6715
Joel Johansson https://orcid.org/0000-0001-5975-290X

References

Abolfathi, B., Aguado, D. S., Aguilar, G., et al. 2018, ApJS, 235, 42
Alard, C. 2000, A&AS, 144, 363
Alard, C., & Lupton, R. H. 1998, ApJ, 503, 325
Alexander, K. D., Berger, E., Guillochon, J., Zauderer, B. A., & Williams, P. K. G. 2016, ApJL, 819, L25
Almeida, A., Anderson, S. F., Argudo-Fernández, M., et al. 2023, ApJS, 267, 44
Arcavi, I. 2022, ApJ, 937, 75
Arcavi, I., Gal-Yam, A., Sullivan, M., et al. 2014, ApJ, 793, 38
Bade, N., Komossa, S., & Dahlem, M. 1996, A&A, 309, L35
Baldwin, J. A., Phillips, M. M., & Terlevich, R. 1981, PASP, 93, 5
Barbarino, C., Carracedo, A. S., Tartaglia, L., & Yaron, O. 2019, TNSCR 2019-287
Becker, A. 2015, HOTPANTS: High Order Transform of PSF ANd Template Subtraction, Astrophysics Source Code Library, ascl:1504.004
Bellm, E. C., Kulkarni, S. R., Graham, M. J., et al. 2019, PASP, 131, 018002
Bennett, C. L., Larson, D., Weiland, J. L., & Hinshaw, G. 2014, ApJ, 794, 135
Blagorodnova, N., Gezari, S., Hung, T., et al. 2017, ApJ, 844, 46
Bogdanović, T., Eracleous, M., Mahadevan, S., Sigurdsson, S., & Laguna, P. 2004, ApJ, 610, 707
Bowen, I. S. 1934, PASP, 46, 146
Bowen, I. S., & Vaughan, A. H. 1973, ApOpt, 12, 1430
Brown, J. S., Holoien, T. W. S., Auchettl, K., et al. 2017, MNRAS, 466, 4904
Brown, T. M., Baliber, N., Bianco, F. B., et al. 2013, PASP, 125, 1031
Bu, D.-F., Chen, L., Mou, G., Qiao, E., & Yang, X.-H. 2023, MNRAS, 521, 4180
Buzzoni, B., Delabre, B., Dekker, H., et al. 1984, Msngr, 38, 9
Cackett, E. M., Horne, K., & Winkler, H. 2007, MNRAS, 380, 669
Callow, J., Graur, O., Clark, P., et al. 2024, arXiv:2402.16951
Cappelluti, N., Ajello, M., Rebusco, P., et al. 2009, A&A, 495, L9
Cardelli, J. A., Clayton, G. C., & Mathis, J. S. 1989, ApJ, 345, 245
Cendes, Y., Berger, E., Alexander, K. D., et al. 2022, ApJ, 938, 28
Charalampopoulos, P., Leloudas, G., Malesani, D. B., et al. 2022, A&A, 659, A34
Charalampopoulos, P., Pursiainen, M., Leloudas, G., et al. 2023, A&A, 673, A95
Clark, P., Graur, O., Callow, J., et al. 2024, MNRAS, 528, 7076
Coughlin, E. R., & Nixon, C. J. 2019, ApJL, 883, L17
Coughlin, E. R., & Nixon, C. J. 2022, ApJ, 936, 70
Dai, L., McKinney, J. C., Roth, N., Ramirez-Ruiz, E., & Miller, M. C. 2018, ApJL, 859, L20
Demircan, O., & Kahraman, G. 1991, Ap&SS, 181, 313
D'Orazio, D. J., Loeb, A., & Guillochon, J. 2019, MNRAS, 485, 4413
Evans, C. R., & Kochanek, C. S. 1989, ApJL, 346, L13
Filippenko, A. V. 1982, PASP, 94, 715
Fitzpatrick, E. L. 1999, PASP, 111, 63
Frank, J., & Rees, M. J. 1976, MNRAS, 176, 633
French, K. D., & Zabludoff, A. I. 2018, ApJ, 868, 99
Gafton, E., Tejeda, E., Guillochon, J., Korobkin, O., & Rosswog, S. 2015, MNRAS, 449, 771
Gezari, S. 2021, ARA&A, 59, 21
Gezari, S., Chornock, R., Lawrence, A., et al. 2015, ApJL, 815, L5
Gezari, S., Chornock, R., Rest, A., et al. 2012, Natur, 485, 217
Gezari, S., Martin, D. C., Milliard, B., et al. 2006, ApJL, 653, L25
Goodwin, A. J., van Velzen, S., Miller-Jones, J. C. A., et al. 2022, MNRAS, 511, 5328
Green, G. M., Schlafly, E. F., Finkbeiner, D., et al. 2018, MNRAS, 478, 651
Greene, J. E., & Ho, L. C. 2007, ApJ, 667, 131
Guillochon, J., Manukian, H., & Ramirez-Ruiz, E. 2014, ApJ, 783, 23
Guillochon, J., Nicholl, M., Villar, V. A., et al. 2018, ApJS, 236, 6
Guillochon, J., & Ramirez-Ruiz, E. 2013, ApJ, 767, 25
Gültekin, K., Richstone, D. O., Gebhardt, K., et al. 2009a, ApJ, 695, 1577
Gültekin, K., Richstone, D. O., Gebhardt, K., et al. 2009b, ApJ, 698, 198
Hammerstein, E., van Velzen, S., Gezari, S., et al. 2023, ApJ, 942, 9
Heikkila, T., Reynolds, T., Kankare, E., et al. 2019, ATel, 12529, 1
Henden, A. A., Templeton, M., Terrell, D., et al. 2016, yCat, 2336, 0
Hinkle, J. T., Holoien, T. W. S., Auchettl, K., et al. 2021a, MNRAS, 500, 1673
Hinkle, J. T., Holoien, T. W. S., Shappee, B. J., & Auchettl, K. 2021b, ApJ, 910, 83

Hodgkin, S. T., Harrison, D. L., Breedt, E., et al. 2021, A&A, 652, A76
Holoien, T. W. S., Auchettl, K., Tucker, M. A., et al. 2020, ApJ, 898, 161
Holoien, T. W. S., Huber, M. E., Shappee, B. J., et al. 2019a, ApJ, 880, 120
Holoien, T. W. S., Kiyota, S., Brimacombe, J., et al. 2014a, ATel, 6732, 1
Holoien, T. W. S., Kochanek, C. S., Prieto, J. L., et al. 2016a, MNRAS, 463, 3813
Holoien, T. W. S., Kochanek, C. S., Prieto, J. L., et al. 2016b, MNRAS, 455, 2918
Holoien, T. W. S., Prieto, J. L., Bersier, D., et al. 2014b, MNRAS, 445, 3263
Holoien, T. W. S., Vallely, P. J., Auchettl, K., et al. 2019b, ApJ, 883, 111
Horesh, A., Cenko, S. B., & Arcavi, I. 2021, NatAs, 5, 491
Horne, K. 1986, PASP, 98, 609
Huang, S., Jiang, N., Shen, R.-F., Wang, T., & Sheng, Z. 2023, ApJL, 956, L46
Hung, T., Gezari, S., Blagorodnova, N., et al. 2017, ApJ, 842, 29
Komossa, S., & Greiner, J. 1999, A&A, 349, L45
Komossa, S., Zhou, H., Wang, T., et al. 2008, ApJL, 678, L13
Kormendy, J., & Ho, L. C. 2013, ARA&A, 51, 511
Krolik, J., Piran, T., Svirski, G., & Cheng, R. M. 2016, ApJ, 827, 127
Leloudas, G., Bulla, M., Cikota, A., et al. 2022, NatAs, 6, 1193
Leloudas, G., Dai, L., Arcavi, I., et al. 2019, ApJ, 887, 218
Leloudas, G., Fraser, M., Stone, N. C., et al. 2016, NatAs, 1, 0002
Lightman, A. P., & Shapiro, S. L. 1977, ApJ, 211, 244
Liu, X.-L., Dou, L.-M., Chen, J.-H., & Shen, R.-F. 2022, ApJ, 925, 67
Mainetti, D., Lupi, A., Campana, S., et al. 2017, A&A, 600, A124
Mainzer, A., Bauer, J., Cutri, R. M., et al. 2014, ApJ, 792, 30
Mainzer, A., Grav, T., Bauer, J., et al. 2011, ApJ, 743, 156
Maksym, W. P., Lin, D., & Irwin, J. A. 2014, ApJL, 792, L29
Masci, F. J., Laher, R. R., Rusholme, B., et al. 2019, PASP, 131, 018003
McCully, C., Volgenau, N. H., Harbeck, D.-R., et al. 2018, Proc. SPIE, 10707, 107070K
Merritt, D. 2013, CQGra, 30, 244005
Miles, P. R., Coughlin, E. R., & Nixon, C. J. 2020, ApJ, 899, 36
Miller, J. S., & Stone, R. P. S. 1994, Lick Obs. Tech. Rep. 66, Santa Cruz: Lick Obs.
Mockler, B., Guillochon, J., & Ramirez-Ruiz, E. 2019, ApJ, 872, 151
Mockler, B., & Ramirez-Ruiz, E. 2021, ApJ, 906, 101
Mullaney, J. R., Alexander, D. M., Fine, S., et al. 2013, MNRAS, 433, 622
Newsome, M., Arcavi, I., Howell, D. A., et al. 2024, ApJ, 961, 239
Nicholl, M. 2018, RNAAS, 2, 230
Nicholl, M., Lanning, D., Ramsden, P., et al. 2022, MNRAS, 515, 5604
Oke, J. B. 1974, ApJS, 27, 21
Onori, F., Cannizzaro, G., Jonker, P. G., et al. 2019, MNRAS, 489, 1463
Onori, F., Cannizzaro, G., Jonker, P. G., et al. 2022, MNRAS, 517, 76
Pasham, D. R., Cenko, S. B., Sadowski, A., et al. 2017, ApJL, 837, L30
Payne, A. V., Auchettl, K., Shappee, B. J., et al. 2023, ApJ, 951, 134
Payne, A. V., Shappee, B. J., Hinkle, J. T., et al. 2021, ApJ, 910, 125
Payne, A. V., Shappee, B. J., Hinkle, J. T., et al. 2022, ApJ, 926, 142
Peterson, B. M., Wanders, I., Horne, K., et al. 1998, PASP, 110, 660
Phinney, E. S. 1989, in IAU Symp. 136, The Center of the Galaxy, ed. M. Morris (Dordrecht: Kluwer), 543
Piran, T., Svirski, G., Krolik, J., Cheng, R. M., & Shiokawa, H. 2015, ApJ, 806, 164
Poole, T. S., Breeveld, A. A., Page, M. J., et al. 2008, MNRAS, 383, 627
Rees, M. J. 1988, Natur, 333, 523
Reines, A. E., & Volonteri, M. 2015, ApJ, 813, 82
Roming, P. W. A., Kennedy, T. E., Mason, K. O., et al. 2005, SSRv, 120, 95
Roth, N., & Kasen, D. 2018, ApJ, 855, 54
Roth, N., Kasen, D., Guillochon, J., & Ramirez-Ruiz, E. 2016, ApJ, 827, 3
Ryu, T., Krolik, J., & Piran, T. 2020, ApJ, 904, 73
Sand, D. J., Brown, T., Haynes, R., & Dubberley, M. 2011, AAS Meeting, 218, 132.03
Saxton, R., Komossa, S., Auchettl, K., & Jonker, P. G. 2020, SSRv, 216, 85
Schlafly, E. F., & Finkbeiner, D. P. 2011, ApJ, 737, 103
Sfaradi, I., Horesh, A., Fender, R., et al. 2022, ApJ, 933, 176
Shappee, B. J., Prieto, J. L., Grupe, D., et al. 2014, ApJ, 788, 48
Short, P., Lawrence, A., Nicholl, M., et al. 2023, MNRAS, 525, 1568
Silverman, J. M., Ganeshalingam, M., Li, W., & Filippenko, A. V. 2012, MNRAS, 425, 1889
Smartt, S. J., Valenti, S., Fraser, M., et al. 2015, A&A, 579, A40
Smith, K. W., Smartt, S. J., Young, D. R., et al. 2020, PASP, 132, 085002
Speagle, J. S. 2020, MNRAS, 493, 3132
Stanek, K. Z. 2019, TNSTR, 2019-262, 1
Steinberg, E., & Stone, N. C. 2024, Natur, 625, 463
Stern, D., Assef, R. J., Benford, D. J., et al. 2012, ApJ, 753, 30
Stone, N. C., & Metzger, B. D. 2016, MNRAS, 455, 859
STScI Development Team 2013, pysynphot: Synthetic Photometry Software Package, Astrophysics Source Code Library, ascl:1303.023
STScI Development Team 2018, synphot: Synthetic Photometry using Astropy, Astrophysics Source Code Library, ascl:1811.001
Tody, D. 1986, Proc. SPIE, 627, 733
Tody, D. 1993, in ASP Conf. Ser. 52, Astronomical Data Analysis Software and Systems II, ed. R. J. Hanisch, R. J. V. Brissenden, & J. Barnes (San Francisco, CA: ASP), 173
Tonry, J. L., Denneau, L., Heinze, A. N., et al. 2018, PASP, 130, 064505
Ulmer, A. 1999, ApJ, 514, 180
Valenti, S., Howell, D. A., Stritzinger, M. D., et al. 2016, MNRAS, 459, 3939
van Dokkum, P. G. 2001, PASP, 113, 1420
van Velzen, S., Anderson, G. E., Stone, N. C., et al. 2016, Sci, 351, 62
van Velzen, S., Farrar, G. R., Gezari, S., et al. 2011, ApJ, 741, 73
van Velzen, S., Gezari, S., Hammerstein, E., et al. 2021, ApJ, 908, 4
van Velzen, S., Gezari, S., Hung, T., et al. 2019, ATel, 12568, 1
van Velzen, S., Holoien, T. W. S., Onori, F., Hung, T., & Arcavi, I. 2020, SSRv, 216, 124
Wang, T.-G., Zhou, H.-Y., Komossa, S., et al. 2012, ApJ, 749, 115
Wang, Y., Baldi, R. D., del Palacio, S., et al. 2023, MNRAS, 520, 2417
Wevers, T. 2020, MNRAS, 497, L1
Wevers, T., Nicholl, M., Guolo, M., et al. 2022, A&A, 666, A6
Will, C. M. 2012, CQGra, 29, 217001
Wright, E. L. 2006, PASP, 118, 1711
Wright, E. L., Eisenhardt, P. R. M., Mainzer, A. K., et al. 2010, AJ, 140, 1868
Yang, C.-W., Wang, T.-G., Ferland, G., et al. 2013, ApJ, 774, 46
Yaron, O., & Gal-Yam, A. 2012, PASP, 124, 668
Yuan, H. B., Liu, X. W., & Xiang, M. S. 2013, MNRAS, 430, 2188